AGU PUBLICATIONS

JGR

Journal of Geophysical Research: Atmospheres

RESEARCH ARTICLE
10.1002/2017JD027303

Key Points:
- Observation of mountain wave breakdown in upper mesosphere
- Observations of vortex dynamics leading to turbulence
- Vortex dynamics predicted by direct numerical simulations

Supporting Information:
- Supporting Information S1
- Movie S1

Correspondence to:
J. H. Hecht,
james.hecht@aero.org

Citation:
Hecht, J. H., Fritts, D. C., Wang, L., Gelinas, L. J., Rudy, R. J., Walterscheid, R. L., … Franke, S. J. (2018). Observations of the breakdown of mountain waves over the Andes Lidar Observatory at Cerro Pachon on 8/9 July 2012. *Journal of Geophysical Research: Atmospheres*, *123*, 276–299. https://doi.org/10.1002/2017JD027303

Received 14 JUN 2017
Accepted 30 NOV 2017
Accepted article online 7 DEC 2017
Published online 15 JAN 2018

Observations of the Breakdown of Mountain Waves Over the Andes Lidar Observatory at Cerro Pachon on 8/9 July 2012

J. H. Hecht[1], D. C. Fritts[2], L. Wang[2], L. J. Gelinas[1], R. J. Rudy[1], R. L. Walterscheid[1], M. J. Taylor[3], P. D. Pautet[3], S. Smith[4], and S. J. Franke[5]

[1]Space Science Applications Laboratory, Aerospace Corporation, El Segundo, CA, USA, [2]GATS Inc., Boulder, CO, USA, [3]Center for Atmospheric and Space Sciences, Utah State University, Logan, UT, USA, [4]Center for Space Physics, Boston University, Boston, MA, USA, [5]Electrical and Computer Engineering, University of Illinois, Urbana, IL, USA

Abstract Although mountain waves (MWs) are thought to be a ubiquitous feature of the wintertime southern Andes stratosphere, it was not known whether these waves propagated up to the mesopause region until Smith et al. (2009) confirmed their presence via airglow observations. The new Andes Lidar Observatory at Cerro Pachon in Chile provided the opportunity for a further study of these waves. Since MWs have near-zero phase speed, and zero wind lines often occur in the winter upper mesosphere (80 to 100 km altitude) region due to the reversal of the zonal mean and tidal wind, MW breakdown may routinely occur at these altitudes. Here we report on very high spatial/temporal resolution observations of the initiation of MW breakdown in the mesopause region. Because the waves are nearly stationary, the breakdown process was observed over several hours; a much longer interval than has previously been observed for any gravity wave breakdown. During the breakdown process observations were made of initial horseshoe-shaped vortices, leading to successive vortex rings, as is also commonly seen in Direct Numerical Simulations (DNS) of idealized and multiscale gravity wave breaking. Kelvin-Helmholtz instability (KHI) structures were also observed to form. Comparing the structure of observed KHI with the results of existing DNS allowed an estimate of the turbulent kinematic viscosity. This viscosity was found to be around 25 m^2/s, a value larger than the nominal viscosity that is used in models.

1. Introduction

Two of the main sources of atmospheric gravity waves (AGWs) in the middle to upper atmosphere are thought to be (a) convective activity in the troposphere and (b) air flow over topography producing mountain waves (MWs) (Fritts & Alexander, 2003). Convective generation produces AGWs that propagate both horizontally and vertically and have been routinely observed via airglow imaging in the UMLT region (the upper mesosphere and lower thermosphere from about 80 to 100 km altitude). Orographic generation produces AGWs that are nearly stationary horizontally in the ground-based frame of reference, a practical definition of MWs. They propagate horizontally and vertically in the intrinsic frame.

A particular hot spot for MW generation is the southern Andes in the June to September period where eastward winds blowing over the Andes produce copious vertically propagating MWs both observationally and in modeling (Jiang et al., 2002; Preusse et al., 2002; Sato et al., 2012). These waves most often have phase fronts aligned with the crest of the Andes, essentially N-S. In cases where the MW phases are found not to be aligned nearly N-S, these orientations can be due to variations in the local terrain direction, or to advection or refraction to other orientations by the mean wind, and especially its lateral shear (e.g., see Alexander & Teitelbaum, 2011; Preusse et al., 2002; Sato et al., 2012). The latter study showed that the shorter horizontal wavelength waves (which are the hardest to observe from satellites) tend to stay over the highest terrain. How and at what altitude MWs dissipate, and thus whether they reach the UMLT region, was an open question until 2009 when Smith et al. (2009) used airglow imaging to observe MWs during several nights of July 2008 from El Leoncito, Argentina (31.8°S, 69.3°W), an observatory east of the Andes crest.

The fact that airglow observations can measure MWs opens up several additional research topics that can be addressed by that technique. Because of their high spatial resolution (much better than 1 km), these imagers

can see the small-scale MWs that are not visible by satellite remote sensing. A large fraction of the total energy and momentum deposited by gravity waves into the atmosphere may be due to these small-scale waves.

While MWs are roughly stationary to a ground-based observer, the instability dynamics are not and normally get advected with the mean and MW wind field once formed. The ability to watch the evolutions of these flows is possible when an airglow imager field of view is sufficiently large to allow for some advection over the course of the instability evolution. Thus, if MWs break down, there are opportunities for detailed temporal and spatial studies of the wave breakdown process and the transition to turbulence.

Instabilities and turbulence accompanying unstable AGWs have been of interest for many years. Initial and more recent numerical studies revealed the dynamics underlying AGW breaking in sheared and unsheared environments (e.g., Achatz, 2005, 2007; Andreassen et al., 1994, 1998; Fritts et al., 1993, 1994, 1996, 1998, 2009a, 2009b; Walterscheid & Schubert, 1990). More recent modeling studies examined instabilities accompanying superposed mean and AGW motions that we will refer to as multiscale flows hereafter (Fritts et al., 1997, 2009, 2013, 2016). During this time interval there were also multiple observations of AGW instability and related KHI dynamics, often in clear multiscale flows, some of which employed direct numerical simulation (DNS) results to help quantify their interpretations (e.g., Baumgarten & Fritts, 2014; Cai et al., 2014; Fritts et al., 1993, 1997, 2003, 2017; Fritts, Wan, et al., 2014; Hecht et al., 1997, 2004, 2005; Hecht, 2004; Li et al., 2005; Yamada et al., 2001). These various studies laid the groundwork for our applications of DNS results in the interpretation of MW-induced instabilities in this paper.

In 2009 the Andes Lidar Observatory (ALO) was established near the crest of the Andes at Cerro Pachon Chile (30°S,70°W). ALO includes among its instrument complement a meteor radar and two airglow instruments that can be used to study the lifecycle of Kelvin-Helmholtz Instabilities (KHIs) (Fritts, Wan, et al., 2014; Hecht et al., 2014). One of the airglow imagers has a pixel resolution of 500 m, with images taken every 2 to 4 s, thus providing the best spatial/temporal resolution to date for studying a wave breakdown event in the airglow layer. On the evening of 8–9 July 2012, MWs appeared directly over ALO and were present from about 2230 UT on 8 July to almost 0300 UT on 9 July. Around 2310 to 2320 UT the MWs exhibited initial instabilities, and these dynamics were observed for over 2 h.

Data presented here represent the most detailed observations to date of the breakdown of a MW in the upper mesosphere. These data are interpreted with the aid of DNS of AGW and KHI instability dynamics in idealized and multiscale flows cited above. Importantly, two distinct dynamics are suggested by the observations presented here. One indicates MW breaking at a large amplitude; the second indicates a local KHI due to the multiscale superposition of the MW and the vertical shear of the mean horizontal wind.

In the case of idealized or multiscale AGW breaking, there is no specific instability threshold, as multiple studies have revealed that all AGWs are unstable at all amplitudes (Lombard & Riley, 1996; Sonmor & Klaassen, 1997), but rapid instability evolutions only occur for amplitudes approaching overturning. This approach to overturning is quantified by N^2 approaching 0 (Achatz, 2005, 2007; Fritts et al., 1998, 2009a, 2009b), where N is the buoyancy frequency (see section 2.4) and $2\pi/N$ is the buoyancy period T_b. For AGWs having minimum N^2 near 0, initial optimal perturbations lead to approximately shear-aligned counterrotating vortices that interact increasingly as their amplitudes grow. The interactions drive links among adjacent vortices that yield horseshoe-shaped vortices that in turn lead to vortex rings. The vortex rings cause plunging motions, strong additional vortex interactions at smaller scales, and a rapid transition to turbulence thereafter. These dynamics typically span about 3 T_b for large-amplitude AGWs.

In contrast, KHI in idealized plane parallel flows (e.g., Drazin, 1958; Fritts, Baumgarten, et al., 2014; Klaassen & Peltier, 1991; Werne & Fritts, 1999), and where such conditions are approximated locally (e.g., Fritts et al., 2013, 2016; Hecht et al., 2005, 2014; Lelong & Dunkerton, 1998), appear to adhere roughly to the instability threshold inferred for the more idealized cases, for example, a Richardson number $Ri < 1/4$ (see section 2.4). Transitions to turbulence accompanying KHI depend strongly on both Ri and the effective Reynolds number, $Re = Uh/\nu$, where here U is half the horizontal wind variation across the shear layer, h is half the shear depth, and ν is the effective viscosity, either kinematic or turbulent. For Ri near 1/4, KH billows are shallow and evolve slowly, as the available kinetic energy of the shear flow only slightly exceeds that required for billow overturning. At smaller Ri, KH billows are energetic and their depths approach approximately half the horizontal wavelength (Thorpe, 1973). Sensitivity to Re is seen most clearly in the occurrence and scales of secondary KHI accounting for the transition to turbulence (or its absence). At low Ri and moderate Re, these instabilities

comprise streamwise-aligned, counterrotating vortices that arise in the strongly sheared, and variably stratified KH billow exteriors for low *Ri*. At sufficiently high *Re* (larger than roughly 1,000), spanwise instability scales decrease with increasing *Re*; for *Re* of about 1,000 or less, secondary KHI occur at much larger spanwise scales, or are suppressed entirely (Fritts, Baumgarten, et al., 2014). At very high *Re* (roughly 10,000 or larger), secondary KHI can also exhibit smaller-scale KHI on the strongly sheared and stratified braids between adjacent billows (Fritts et al., 2012). The implications of these results are that observed primary KHI depths and secondary KHI spanwise scales and orientations provide strong clues to the *Ri* and *Re* that characterize these events, and thus also to the effective turbulent viscosity.

Given the above, we will assume that the conditions for MW breaking and KHI that apply in our analyses below are when N^2 is approaching zero or *Ri* is less than 0.25, respectively. The calculations of both of these quantities are determined from observations of the wave-induced temperature and wind variations combined with the background flow. This approach allows us to address, in addition to an estimate of turbulent viscosity and insights about vortex ring observations, two related questions. These are (1) why did the MW break down and (2) why did the breakdown event occur just after 2300 UT. The results from this approach, as detailed in the body of this study, are that while the time and altitude of the MW breakdown are dependent on the superposed MW and background flow, they appear to be consistent with these numerical criteria.

2. Instrumentation and Model

2.1. Instrumentation at the Andes Lidar Observatory (30.25°S,70.73°W)

2.1.1. ANI

The Aerospace Corporation's near-IR camera (ANI) is described in some detail in Hecht et al. (2005) and in Hecht et al. (2014). The camera has a wide-angle lens with a 256 by 256 HgCdTe detector array to provide images over an approximate 73 by 73° region of the sky. In an image, 128 pixels across the center is approximately equal to 40°, or 61 km, at 85 km altitude. The array consists of four 128 by 128 quadrants each with their own readout circuitry. A new detector was purchased prior to installation at ALO so that all four quadrants are now operational. A fixed open filter position is used allowing a spectral range of 1.55 to 1.7 μm, determined by the internal filters, to be imaged. This spectral range is dominated by the OH Meinel airglow, and because the OH Meinel (4,2) band brightness is almost 100 kilo-Rayleighs, the signal-to-noise ratio (SNR) for a 1 s integration is over 200:1. In the images east is to the left and north is on top.

Images are presented in one of three ways, the first two of which have been used in previous publications (Hecht et al., 2005, 2007, 2014). (1) Individual images are divided by a composite image that is an average of images taken during a period of low wave activity. This flattens the field and corrects for the varying response across the image. The resultant image shows all the features, but because instabilities tend to have amplitudes of about 1% of the background, the contrast can be poor for such features. (2) An image which is the difference of two images taken about 1 min apart. This eliminates the static background and increases the contrast for fast-moving features such as KHIs. The downside of this approach is that it adds some confusion as to the actual structure of the instability features. (3) A new mode where an MW image taken at the beginning of the night, before wave breakdown occurred, is subtracted from all subsequent images. This has some of the benefits of (1) and (2) without adding to the confusion noted in (2). Examples of all three approaches will be presented below.

2.1.2. MTM

To determine the temperature perturbations induced by atmospheric gravity wave activity, some data are used from the Utah State University Mesospheric Temperature Mapper (MTM) that has been designed to measure the mesospheric OH (6,2) rotational temperatures over a 90° field of view, centered on the zenith. It uses (1) a back-illuminated 1024 by 1024 pixel CCD detector that is binned down to 128 by 128 pixels to improve the sensitivity, (2) a Keo Scientific telecentric lens system, and (3) a set of narrowband interference filters to measure the P12 and P14 lines of the OH (6,2) band, and the sky background (BG) intensity at 857 nm (Taylor et al., 2001). The three filters (P12, P14, and BG) were exposed for 30 s each, providing a temperature map every 1.75 min. The zenith temperature data, obtained by dividing the background-corrected OH filter images, correspond to the average of a small 5 by 5 pixel area (approximately 4 by 4°).

2.1.3. Meteor Radar

Wind data are available from the UIUC meteor radar (MR) located at the base of Cerro Pachon. This instrument is fully described in Franke et al. (2005). A single three-element Yagi antenna directed toward the zenith is used to illuminate meteor trails. Meteor trail reflections are coherently detected on five three-element Yagi

antennas oriented along two orthogonal baselines, with one antenna in the center of the array common to both baselines. On each baseline the outer antennas are separated from the center antenna by 1.5 and 2.0 wavelengths. This configuration minimizes antenna coupling, provides enough redundancy to unambiguously determine the azimuth and elevation of most echoes, and provides excellent angular resolution for position determination. For this study, points were provided every half hour in the altitude range 80 to 100 km, and sampled every 1 km. The altitude resolution of these estimates is determined by a triangular weighting function, with a half width of 3 km and a base width of 6 km.

2.2. Instrumentation at the El Leoncito Observatory (31.80°S,69.28°W)

The El Leoncito Observatory is approximately 220 km to the southeast of ALO.

2.2.1. Airglow Imager at the El Leoncito Observatory

The Boston University all-sky imager (Martinis et al., 2006; Smith et al., 2006, 2009) utilizes an Andor 2048 by 2048 pixel bare-CCD camera, cooled to −50°C, and fitted with a 16 mm fish-eye lens which affords an all-sky (180°) view of the nighttime sky. Several nighttime emissions from the upper mesosphere (80–100 km) are recorded using a series of narrowband (1.2–1.8 nm) filters: Na (589.3 nm), and O(^{1}S) (557.7 nm) and OH (broadband IR, 695–1050 nm). Nightly observations were made during clear, moonless periods, with each filter being cycled sequentially. The integration times were 90 s, except for the OH filter (30 s).

The raw all-sky images were processed using a standard procedure; first, initial bias and dark subtraction, and then flat fielding to remove effects of vignetting due to the imaging system, atmospheric extinction, and van Rhijn brightening. A routine was also used to remove stars and reduce the effect of the Milky Way. The images were then calibrated photometrically into Rayleigh (*R*) brightness units. Finally, the images were mapped onto geographic coordinates using the nominal heights of the emission layers, a process called unwarping. The assumed heights used for the OH, Na, and O(^{1}S) emissions were 87, 90, and 96 km, respectively.

2.3. The SABER Instrument on the TIMED Satellite

The Sounding of the Atmosphere using Broadband Emission Radiometry (SABER) experiment is one of four instruments on the Thermosphere Ionosphere Mesosphere Energetics and Dynamics (TIMED) satellite (Russell et al., 1999). SABER scans the atmospheric limb vertically and observes emission in 10 broadband spectral channels. Version 1.07 kinetic temperatures are retrieved from CO_2 15 μm limb emission measurements at approximately 2 km vertical resolution (Mertens et al., 2001).

2.4. Model Simulations

Multiple previous DNS provided guidance for our interpretation of the MW instability dynamics observed in the OH airglow layer over ALO, and described in this paper. These include DNS of idealized AGW breaking and KHI, and of multiscale dynamics arising from AGW and mean shear superpositions. The AGW breaking cases were described by Fritts et al. (2009a, 2009b), the KHI events for various Richardson numbers, *Ri*, and *Re* were described by Fritts et al. (2012, 2009b) and Fritts, Wan et al. (2014), and the multiscale dynamics cases for two *Re* were described by Fritts et al. (2013, 2016). Collectively, these DNS span AGW amplitudes expected to contribute most strongly to wave breaking dynamics, and the ranges of *Ri* and *Re* that are most likely to characterize KHI at airglow altitudes, based on observations at OH airglow altitudes to date.

The relevant *Ri* for the KHI DNS is defined as

$$Ri = \frac{N^2}{(dU/dz)^2} = \frac{(g/T)(dT/dz + g/C_p)}{(dU/dz)^2} \quad (1)$$

where here dU/dz is the mean vertical shear of the total horizontal wind, g is the gravitational acceleration, T is temperature, and C_p is the specific heat at constant pressure.

All DNS employed the NWRA "Triple" pseudo spectral code that solves the Boussinesq Navier-Stokes equations in a triply periodic domain. Applications to AGW breaking employed (a) a computational domain aligned along the AGW phase in order to limit its horizontal extent, (b) an assumed AGW frequency $\omega = N/3.2$, and (c) AGW amplitudes of $a = |u'/c| = 0.9$ and 1.1 for horizontal perturbation velocity u' and phase speed c, corresponding to amplitudes slightly convectively stable and unstable, respectively (see Fritts et al., 2009a for additional details).

Applications to KHI employed a horizontal domain and cosine transforms in altitude, enabling a periodic vertical gradient of the mean horizontal wind and free-slip upper and lower boundaries. These DNS employed a representative horizontal velocity profile given by $U(z) = U\tanh[(z - z_0)/h]$, where here U is the half width

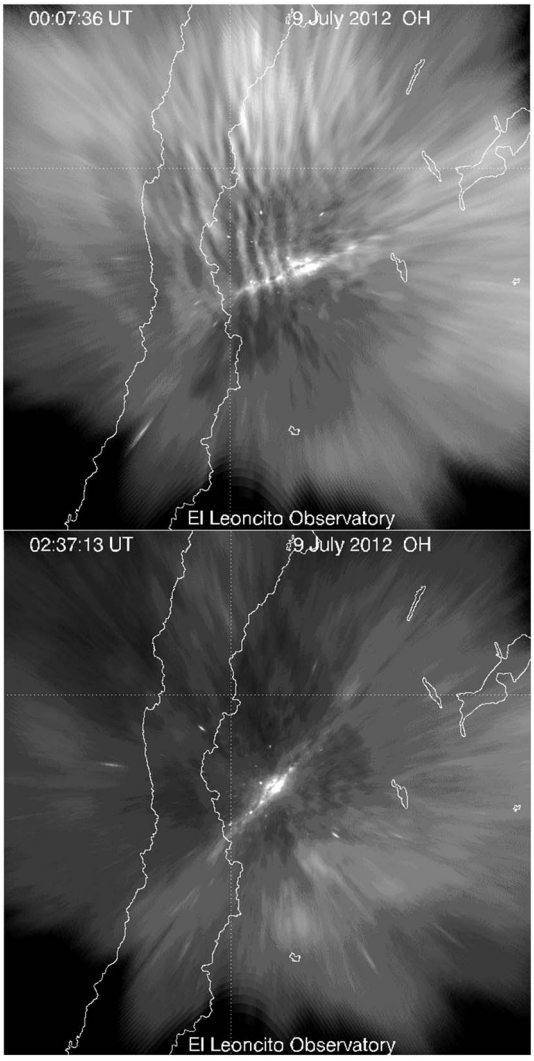

Figure 1. Two panel plots of OH airglow images taken at (top) 2354 UT on 8 July and at (bottom) 0246 UT on 9 July with the camera at El Leoncito. On each image the 30°S latitude and 70°W longitude lines are shown. The images are unwarped to take out the lens distortion.

of the mean wind variation, z_0 is at the center of the vertical domain, and h is the half-depth of the mean wind shear. Additional details of these DNS and their results to which we will refer below are described by Fritts, Wan et al. (2014) and Fritts, Baumgarten, et al., (2014).

Multiscale DNS addressed the AGW and instability dynamics arising from an initial superposition of (a) an AGW having $\omega = N/10$ and $a = 0.5$ and (b) a mean fine-structure shear having a vertical wavelength λ_z roughly one fifth that of the AGW and a minimum $Ri = 0.25$. These yielded complex dynamics that closely resemble AGW and instability dynamics, atmospheric structure, and turbulence statistics seen from near the surface to the upper mesosphere (Fritts et al., 2016, 2017; Miller et al., 2015).

Finally, each of the above categories of DNS has been employed to aid previous analyses of small-scale AGW and instability dynamics observed in OH airglow or polar mesospheric cloud (PMC) displays. In each application, the relevant DNS was used to generate predicted airglow or PMC images for comparisons with the observations, assuming Gaussian brightness variations in altitude and typical airglow or PMC brightness layer depths (e.g., Fritts, Wan, et al., 2014; Fritts, Baumgarten, et al., 2014; Fritts et al., 2017; Miller et al., 2015). Our application here departs from these previous efforts by employing a much thinner assumed OH layer sensitivity (i.e., 3 km), intended to account for the image differencing used to highlight the spatial structures and temporal evolutions of the various events examined. Representative AGW breaking dynamics and their implied OH signatures, intended to aid our analyses, are shown later in section 4.3 (see Figure 14).

2.5. Vertical Wavelength, λ_z

Consider an AGW at an altitude z above its source, in an atmosphere where H is the atmospheric scale height. The vertical wave number, m is given by $2\pi/\lambda_z$ where λ_z is the vertical wavelength. For the MW in this paper, whose intrinsic frequency is well above the inertial frequency but well below the acoustic wave regime, and whose phase velocity is well below the speed of sound, the vertical wave number obeys the following dispersion relation.

$$m^2 = (2\pi/\lambda_z)^2 = \frac{(N^2 - \omega_I^2)(k^2)}{(\omega_I^2)} \quad (2)$$

In equation (2), ω_I is the intrinsic frequency with respect to a frame of reference that moves with the background wind, and k is the horizontal wave number equal to $2\pi/\lambda_h$ where λ_h is the horizontal wavelength. For a given background wind velocity component, $\bar{u}$, in the direction of horizontal wave propagation, and a wave horizontal phase velocity, c, the Doppler-shifted intrinsic wave phase velocity $(c-\bar{u})$ is equal to $\omega_I\lambda_h/(2\pi)$ or simply λ_h/τ_I, where τ_i is the intrinsic period. The vertical wave number, m, thus depends on the background wind, the background temperature, and the vertical temperature gradient.

There are a few cases in section 3.5 where AGWs with very low background winds are considered. In those cases we used a more general expression for m^2 that includes the inertial frequency, and that is presented in Hecht et al. (2007).

3. Results

This paper focuses on the instabilities arising within a multiscale MW environment, including both the dynamics of idealized wave breaking and the local multiscale KHI. While this is perhaps best seen in the movie, attached as a supporting information file to this paper, the body of this work will present additional images that show the instabilities in more detail.

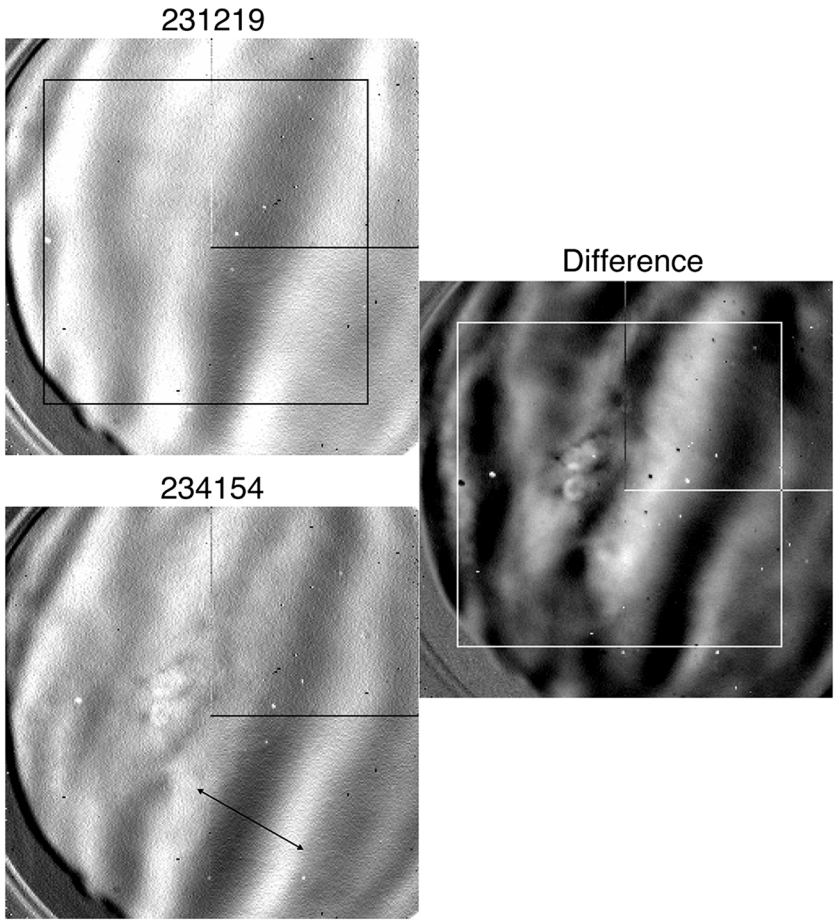

Figure 2. Three panels plot OH images taken by ANI and showing MWs. Each image is 256 × 256 pixels with a pixel equaling approximately 0.5 km at 85 km altitude. The arrow represents a distance of approximately 35 km. North is on top and east is to the left. (top left) 2312 UT showing MWs aligned nearly N/S. (bottom left) 2341 UT showing MWs with their horizontal wavelength spanned by the arrow and showing the beginning of turbulent structures associated with the MW breakdown. (right) Difference between these two images enhancing the contrast of the turbulent structures.

Figure 1 shows two OH images from the BU imager taken just before 0 h UT, and just before 3 h UT on 9 July. The first image clearly shows the presence of stationary waves over both ALO (marked CP for Cerro Pachon) to the northwest, and El Leoncito directly overhead. No MWs are seen in the greenline images which are not shown. This strongly suggests that the MWs have dissipated below 95 km altitude so they do not reach the greenline emission layer, typically near 95 km. By 0247 (2 h 47 min) UT however, the MWs have faded considerably in the OH airglow, suggesting some dissipation or confinement of MW instabilities to altitudes below the OH layer. While the BU imager gives a good overview of the major waves compared to the ANI imager, which observes similar trends in the MW amplitudes, it does not have the temporal resolution to resolve instability dynamics occurring on short time scales.

Figure 2 shows three images from ANI viewing directly over CP. Figure 2 (left column) shows an image at 2312 UT where several phase fronts are seen. These phase fronts stay nearly stationary for several hours. However, by 2341 UT it is clear that in addition to the main MWs, additional structure is present just left of center. To bring out the contrast of this additional structure, the two images are subtracted, following the third new way of image presentation discussed above, and the result is shown in Figure 2 (right). Apparent small-scale (2–3 km) initial instability structures can now be clearly seen, and their evolution and significance will be discussed below. However, in order to interpret these structures, the background atmosphere must first be characterized.

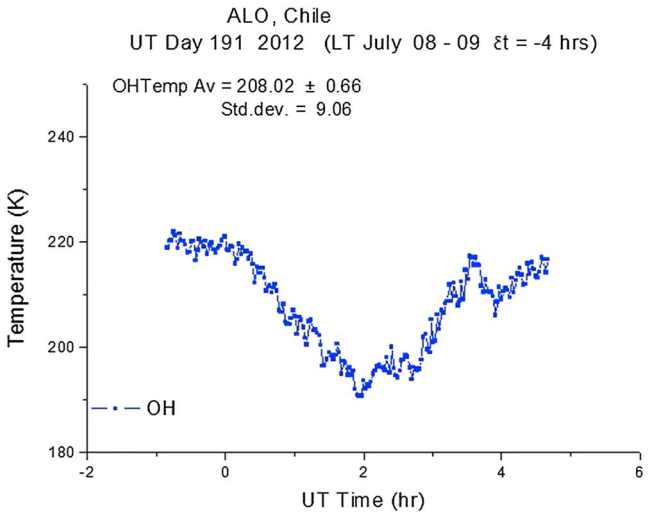

Figure 3. Plot of OH temperature versus time from MTM.

3.1. Airglow Temperature and Brightness

As the initial instability structures appear in the airglow emission, the OH temperature (OHT) can be used to characterize that layer with respect to waves and tides. Figure 3 presents the MTM OHT which is typically close to the temperature at the peak of the layer. Before midnight, around the time where structure appears in the MWs, the OHT is about 220 K.

To further investigate the state of the atmosphere, we show the OHB (OH brightness) from ANI data (Figure 4). The data, shown in Figure 4, are consistently in phase with the OHT data, but because they extend earlier in time, there is a suggestion of a shorter period wavelike feature present prior to 23 UT.

3.2. OH VER and Temperature Profile From SABER

Figure 5 plots the OH volume emission rate (OHVER) in the left column and kinetic temperature in the right column, using data from the SABER instrument on the TIMED satellite. Compared to the ground-based airglow data, these are height resolved and thus show the vertical variation of the OHVER. However, the satellite samples the area around ALO coarsely in space, and for this period three profiles are shown; two of them, at 1955 and 0248 UT, are within 1° in both latitude and longitude of ALO, while the third at 112 UT is 3° south, but about 25° east of the site.

All three time periods show that the OHVER peaks between 80 and 85 km, a few kilometers below the nominal peak at 87 km altitude. They also show a peak in the temperature just above 80 km, with a decrease to a minimum around 95 km. Between these two altitudes there is clearly some structure, indicative of either small vertical wavelength waves, or possibly the horizontal structure of waves that are present during the SABER scan. In the title of the temperature plots an OH temperature is presented, which is the temperature obtained by weighting the temperature profile with the OHVER. For the latter two times these are consistent with the OHT recorded by the airglow instrument. A mean temperature lapse rate can be estimated to be between about −2 to −4 K/km from the altitude of the peak temperature, around 80 to 82 km, to 90 km. This estimate uses a linear fit to the data and assumes that the short scale vertical structure is either contaminated by horizontal structure or not present over Cerro Pachon during the 23 to 24 UT period. Between 80 and 83 km, however, the lapse rate may even be smaller.

3.3. Wind Profiles From the Meteor Radar and the OH Images

The wind profiles are critical to understanding the instabilities seen in the airglow images. A key altitude is the location of the zero wind line (ZWL), the altitude where MWs with zero phase velocity encounter a critical layer. As the ZWL is approached, MWs suffer a reduction in vertical wavelength that can lead to viscous dissipation, and/or the formation of KHIs or overturning, both of which lead to turbulence and wave breakdown. As the MW phases are aligned close to north-south, the ZWL would essentially be the zero wind in the zonal direction.

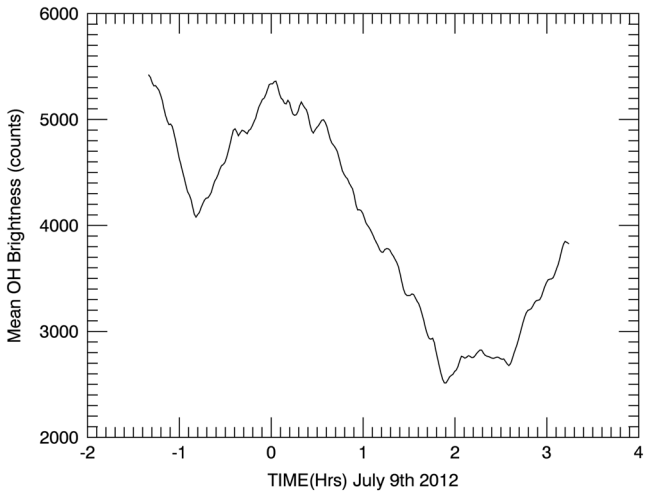

Figure 4. Plot of OH brigthness from ANI data versus time in UT hours referenced to 0 h UT on 9 July 2012.

Figure 6 is a multipanel plot that shows available winds and shears from 22–23 UT on 8 July, to 2–3 UT on 9 July. While the radar winds are not continuous in time, and in fact are absent in the critical 23 to 24 h UT period on 8 July, the available data do allow a reasonable inference of the altitude of the ZWL. Note that these plots do show the winds during some significant periods. These include 22 to 23 UT, the hour before instabilities appeared in the MW OH images, and 0 to 1 UT where bright instability features appear in the images. These instability features are found to gradually diminish from 1 to 3 UT.

The altitude of the ZWL, and the magnitude of the shear on either side of the ZWL, can be determined approximately from these 1 h interval plots. At 22 to 23 UT on 8 July this altitude is located around 91 to 92 km. There is a shear at altitudes just below the ZWL, where the wind velocities

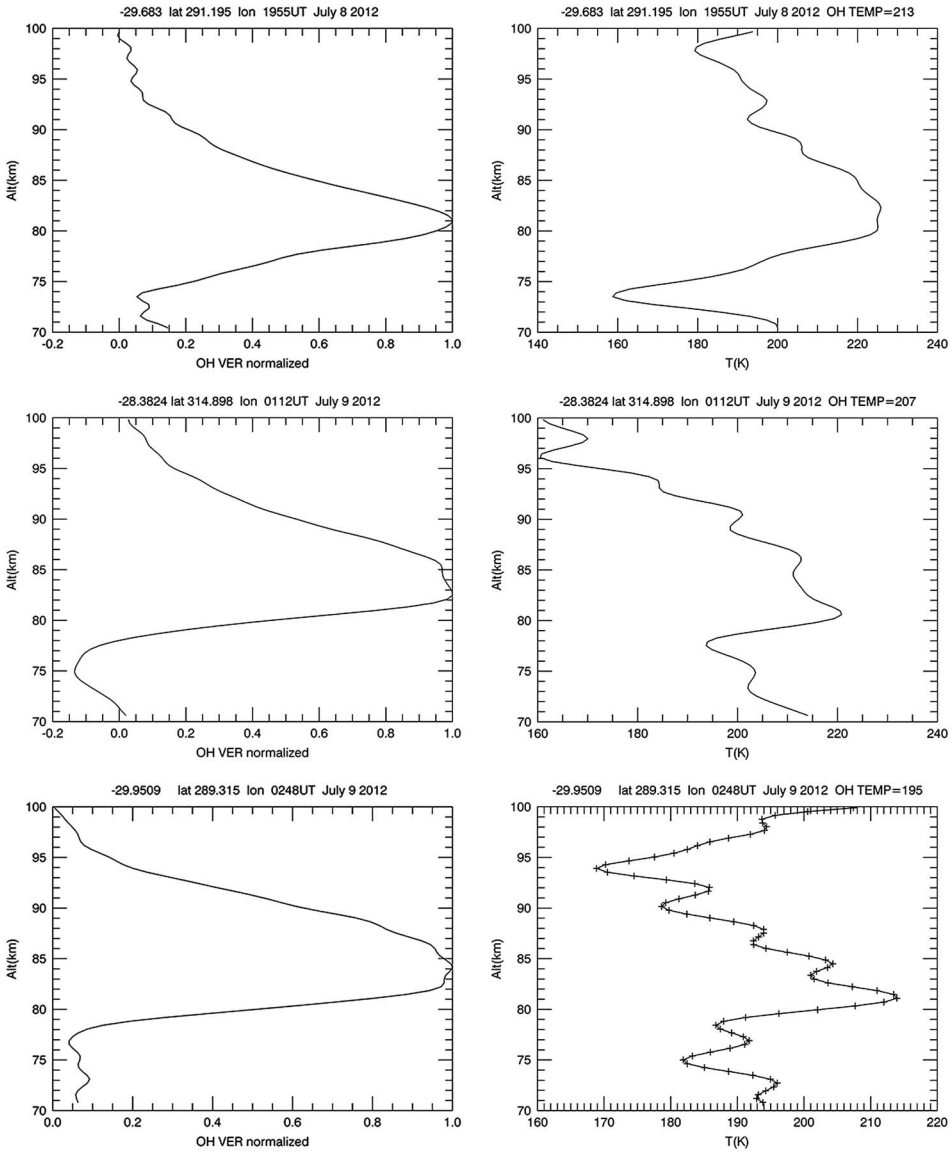

Figure 5. Plot of (left column) SABER OH VER, (right column) temperature at 3 times (top) 1955 UT, (middle) 112 UT, and (bottom) 248 UT. The mean OH Temp in the OHVER is shown in the header. The plus symbols in the Figure 5 (bottom right) show the locations of the actual altitudes used in the SABER data.

are positive reaching 70 m/s by 83 km. At 93 to 94 km, above the ZWL, there is a strong shear of almost 40 m/s/km with westward winds above. Below the ZWL the meridional winds are small.

The other three time intervals are on 9 July. At 0 to 1 UT, an important interval for this study, the ZWL is around 84.5 km, and thus it is moving down in altitude at a rate of 3 to 4 km/h. There is a strong shear almost 2 km in depth around 84 km. The magnitude of the shear is around 30 m/s/km, although given the uncertainty in the wind data this could be as low as 10 m/s/km or as high as 40 m/s/km. The zonal wind speeds are all negative above the shear, and positive, mostly around 30 to 40 m/s, below the shear. The plots at 1 to 2 UT show that the ZWL moves down another 4 km, and at 2 to 3 UT it is no higher than 82 km, and probably lower as the meteor radar data end at 80 km.

The descent of the ZWL and its associated shear is likely due to the downward phase progression of a tide, although a large gravity wave cannot be ruled out. Regardless of the cause, these data are consistent with the altitude of critical layer absorption moving into, and through, the OH emission layer. This explains, as discussed below, the diminished brightness variations of the MWs in the BU and ANI images.

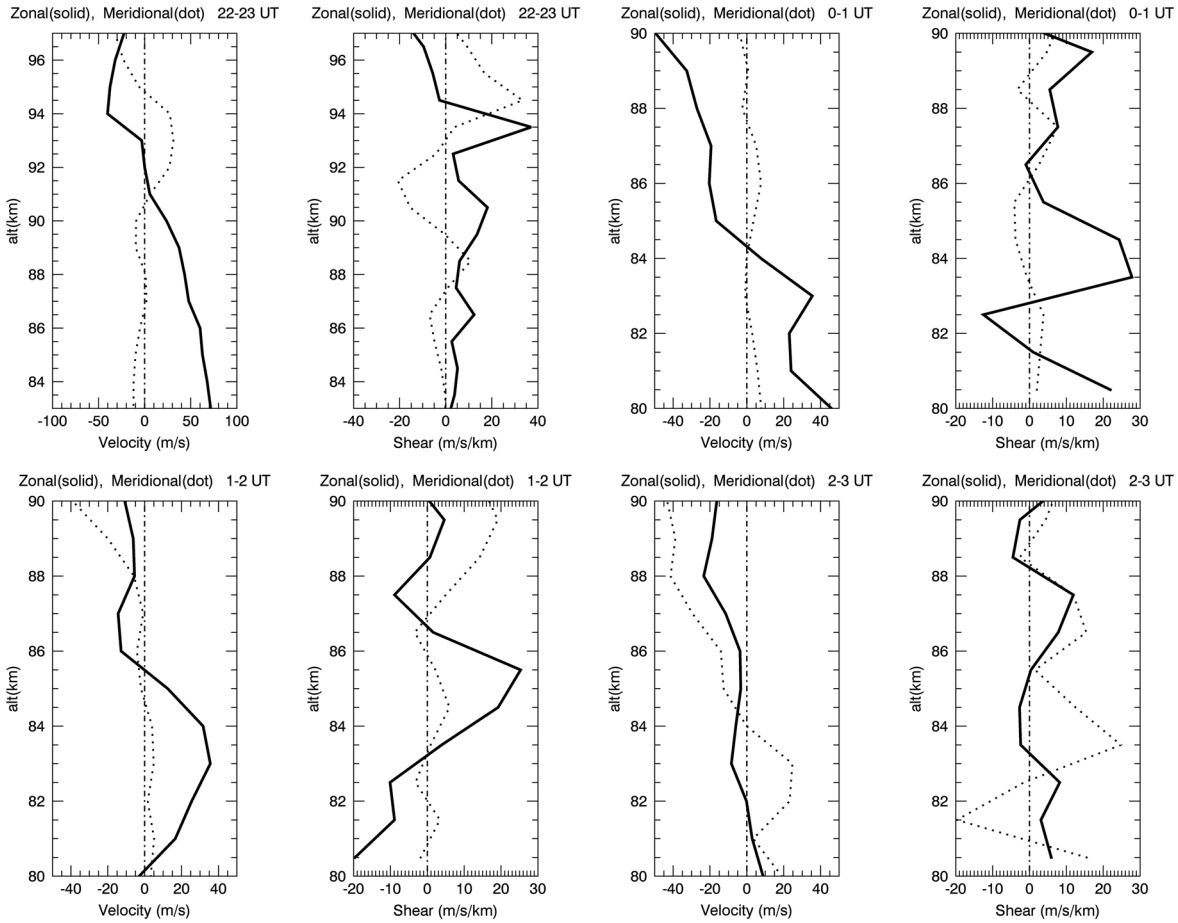

Figure 6. Plots of meteor radar zonal (solid) and meridional (dot) winds and shear versus altitude. The zero line is shown as a dash-dotted line. (top left) 22–23 UT 8 July; (top right) 0–1 UT 9 July; (bottom left) 1–2 UT 9 July; (bottom right) 2–3 UT 9 July.

There is one other piece of information on the wind velocities encountered by the MWs. The ANI images/movie show that the instability features are moving typically around 30 to 40 m/s with some excursions well below or well above these values. They are moving in the nearly eastward direction, thus consistent with winds at an altitude below the ZWL.

3.4. Temperature Perturbation Due To the MW From MTM Images

The MTM instrument also imaged the MWs in temperature as shown previously in Figure 3. The MW temperature perturbations seen in the temperature images were found to be in phase with the intensity perturbations seen in the brightness images. Figure 7 shows a plot of the average temperature amplitude of the MWs, derived from an FFT analysis, versus time. One can calculate the vertical wavelength of the MW knowing its horizontal wavelength, the wind speed in the direction of the wave, and N^2. Given this vertical wavelength (λ_z), and the maximum temperature amplitude (A) of the wave, the maximum lapse rate associated with the wave can be calculated from the following equation

$$dT/dz = \frac{2\pi A}{\lambda_z}. \quad (3)$$

This lapse rate can then be added to the background lapse rate based on the SABER data, and thus N^2 and/or Ri can be calculated that includes both background atmosphere and wave-induced temperature effects.

The difficulty, though, of this approach is that due to wave phase cancellation, the measured temperature amplitude may be considerably different than the actual amplitude. This will be addressed next.

3.5. Mountain Wave Breakdown on Approach to a Critical Layer

An important set of questions arising from the observations are (1) why did the MW break down, and (2) why did the breakdown event occur just after 2300 UT, as shown in the images presented in the next section.

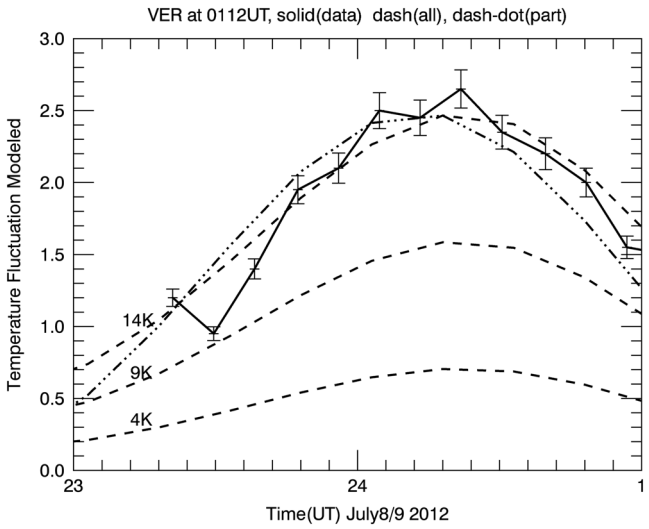

Figure 7. Plot of OH temperature perturbation (solid line) due to a MW versus time from MTM. Dashed lines are model results for a 14 km λ_z with amplitudes of 4, 9, or 14 K. The dash-dotted line is for a 14 K wave with about 1 km less vertical extent in the OHVER (see text).

The answer to both of these questions involves understanding the implications of both the radar wind data discussed in section 3.3 and phase cancellation. In particular, the radar winds show that there is a ZWL descending at a rate of about 4 km/h. Associated with this descent is a shear layer about 1 to 2 km thick, with the wind direction being eastward below the ZWL. Thus, as this layer descends the MW, which has a nearly 0 m/s phase speed, either (a) encounters a critical layer and undergoes viscous dissipation, or (b) on its approach to the critical layer where the MW vertical wavelength decreases, the MW may become unstable due to N^2 approaching zero and the possible formation of a convective instability. However, the airglow is only perturbed by the portion of the MW in its emission layer. Hence, the MW will only be observed to break down when the ZWL enters the airglow layer. This addresses the questions of when and why the MW started to break down.

The descent of the ZWL can be used to quantitatively estimate the amplitude of the MW, provided phase cancellation effects are taken into account. While this is discussed in some detail in Appendix A, the essential results are easy to summarize.

It is well known that airglow imagers and temperature mappers provide brightness and/or temperature perturbations averaged over the airglow layer. This implies phase averaging in the vertical and corresponding underestimates of true AGW brightness and temperature variations when these fields have significant vertical structure at scales comparable to, or less than, the depth of the airglow layer (see, e.g., Swenson & Liu, 1998). This is surely the case in our airglow data set, especially as the ZWL (and the MW critical level) descends into the airglow layer. In such cases, the MW vertical wavelength below the ZWL varies approximately as $\lambda_z = 2\pi U/N$, assuming a hydrostatic MW with ${\lambda_z}^2$ significantly less than ${\lambda_h}^2$. The decreasing U and λ_z imply strong constraints on the MW amplitude below the critical level, as overturning is implied for u′/U approximately 1 (or alternatively a minimum dT/dz approximately $-g/c_p$). Further suppression of transmitted MW amplitudes for mean Ri much greater than 1/4 lead to exponentially smaller MW amplitudes above, and essentially no contribution to airglow brightness modulation above the ZWL (e.g., Hickey et al., 1998). Thus, phase cancellation effects are significant as the descent of the ZWL reduces the effective airglow layer in which the MW resides.

To estimate the cancellation effects, we used the available observations to estimate the vertical wavelength of the MW and then convolved that with the SABER observations of the airglow layer, whose top altitude was determined by the altitude of the descending ZWL. The temperature amplitude and the peak altitude of the MW were then adjusted to best match the airglow observations in Figure 7.

The summary of this analysis suggests several processes that are seen in the data. (1) The variations of the temperature perturbation seen in the MTM data are due, in large part, to variations in wave cancellation as the ZWL descends. (2) Based on (1) the wave amplitude is quite large and thus one would expect instability formation to occur and that direct viscous dissipation of the wave would not be significant. (3) For use later in this study, we note that the vertical wavelength of the MW is 13 to 14 km, and its amplitude is nearly 14 K. These will be used in section 4. (4) This large-amplitude wave probably dissipates shortly after entering the descending shear layer.

3.6. Imaging the Breakdown of a MW

To follow the development of the MW breaking down into turbulence, both a movie and a number of images are shown. The movie, which is shown in the supporting information file and is formed from individual flat-fielded images, begins around 230542 (hhmmss) UT on 8 July, the time just before the MW breakdown process initiated, and when MW phase fronts are easily seen. It then proceeds to show the appearance of organized structures, sometimes exhibiting specific spatial patterns, initially originating at a single location near the center of the image. The features move to the left (eastward), presumably being advected by the background wind, and become less structured and more chaotic prior to their dissipation. The movie continues until around 022527 UT on 9 July, at which time the MWs have completely dissipated. The development of these instabilities, and their evolution and breakdown, are highlighted in Figures 8 to 13. These are all multipanel

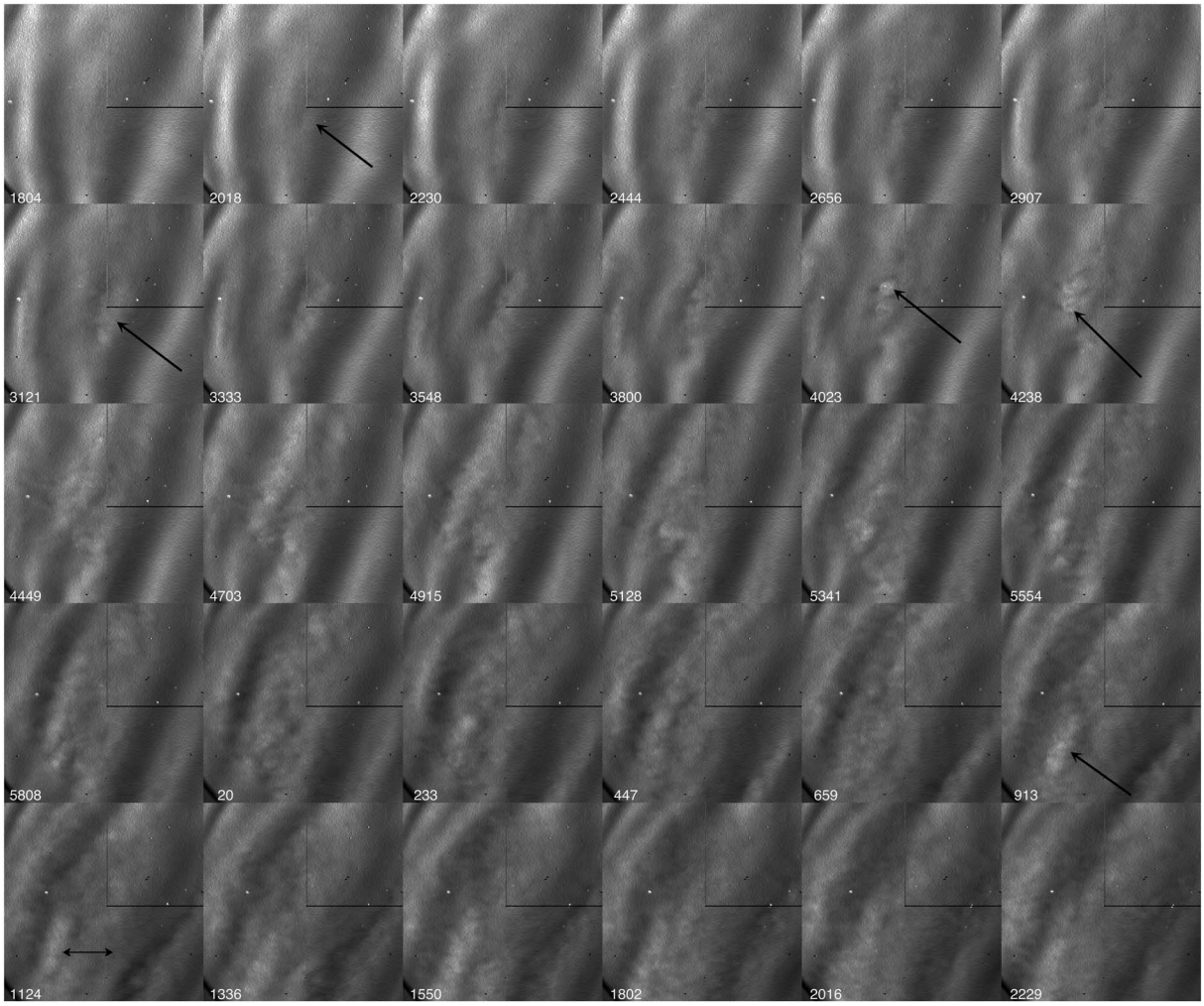

Figure 8. Thirty panels of OH images from ANI. Times increase from left to right, and then top to bottom. Each panel is a raw flatfielded image that consists of the central 200 × 200 pixels. The black arrow in the bottom left panel is 40 pixels long (about 20 km). UTs are from 231804 on 8 July 2012 to 002229 on 9 July 2012, at a little over 2 min intervals. Only minutes and seconds are shown. The single-end black arrows point to interesting features as described in the text.

plots, each using one of the different types of image processing discussed earlier. Figures 12 and 13 also show the formation of KHIs which are not obvious in the movie but resemble those discussed in previous studies (e.g., Hecht et al., 2014).

(1) Figure 8 gives an overview using 30 individual images from the movie (north on top and east to the left). Here each panel in a row is separated by about 2.25 min, and the panels start (top left) at 231804 UT on 8 July, just around the time the MW starts exhibiting instabilities, and ends (bottom right) at 002229 UT on 9 July, as the large-amplitude KHIs are dissipating. Because these use flatfielded images, the contrast of the small-amplitude features is poor. The features can be more easily seen in the movie via their motion. The latter images (Figures 9 to 12) will use differencing techniques to enhance the contrast

The arrows highlight important aspects of the breakdown process. Note that the labels on each panel only show minutes and seconds. Specific features of the evolutions of these features include the following: At 232018 UT the arrow points to a region where the first sign appears of wave-breakdown via the production of initial instability structures. Following the panels until the next arrow, at 233121 UT, shows the development of these instability structures. At 234023 UT a circular blob appears. In the next frame, at 234238 UT, the arrow points to a horseshoe-shaped vortex. Finally, at 000913 UT, the arrow points to a region where large-amplitude KHIs form, as will be shown in Figure 12.

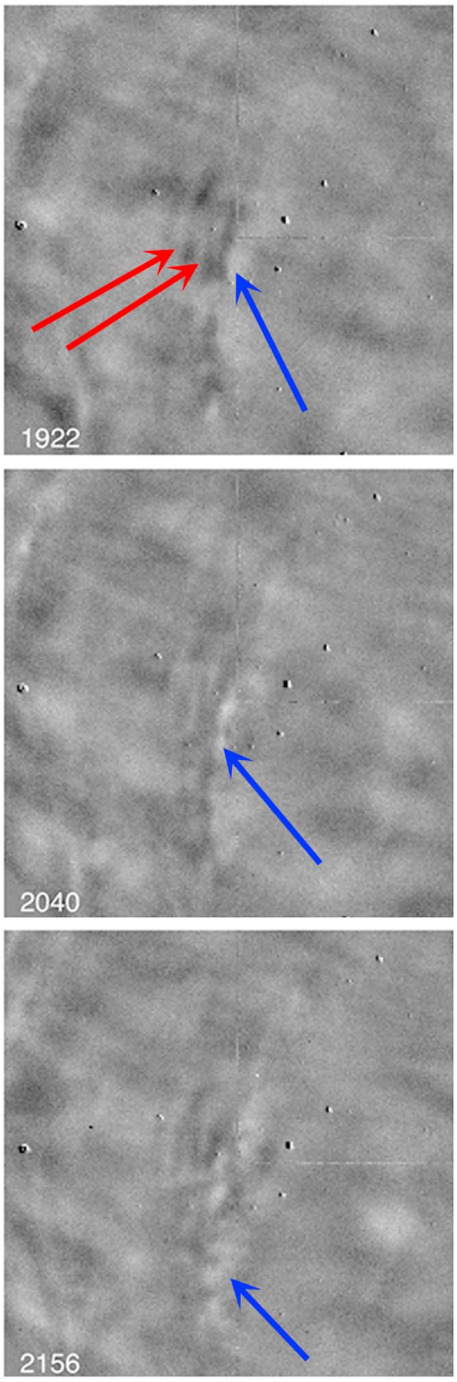

Figure 9. Three panels using 1 min difference images to produce each panel. The period covered is from 231922 to 232156 UT, with panels separated by about 1 and 1/4 min.

(2) Figure 9 shows three panels, each separated by about 1 min, that are processed using the 1 min difference image approach. This approach essentially eliminates any stationary features, such as MWs, but show features that move such as KHIs, MW instability dynamics, or apparent large-scale turbulent structures. This sequence is designed to highlight the period when the first instability features appear.

Important aspects of these images are highlighted by arrows as follows. The red arrows, at 231922 UT, show two KHI phase fronts, which are separated by about 4 to 5 km, suggesting an unstable shear layer thickness less than 1 km (Fritts et al., 1996). These features clearly move to the east (left) with a velocity of 30 to 40 m/s. No secondary perpendicular structures are associated with these KHIs. Because of poor contrast, these small KHIs are not readily visible in the movie.

The blue arrow at 231922 UT highlights the region where instability structures (that are not KHI) first appear. These, as noted above in the Figure 8 discussion, move to the left (eastward) and are seen in the movie. This region appears to be (based on the analysis in Appendix A) at the phase of the wave, as seen from the ground, favorable to forming a convective instability near 90 km as the ZWL descends. This location continues to be the origin of the turbulence for a significant number of frames, which is consistent with our multiscale hypothesis that it is the MW itself combined with the background wind/shear gradient that leads to local instabilities.

Figure 9 (middle), about 1 min later, shows that those instability features now appear as two structures. These two structures are probably the appearance of new features.

The blue arrow in Figure 9 (bottom) at 232156 UT highlights the appearance of a prominent and large horseshoe-shaped vortex feature. The size of this feature is about 5 km and its open end faces nearly east (left) in the direction of the wind. It appears to have formed about 1 min earlier. Further examples will be given in Figures 10 and 11, and a separate section will discuss their significance. The observation of these features near the beginning of the breakdown process is one of the significant aspects of this study.

The instabilities once formed are, as noted above, advected by the wind always nearly eastward at nominal speeds of about 35 m/s, although as noted in section 3.3 there are velocity excursions well above and below this value. Based on the discussion in section 3.5 these wind velocities suggest that these features form at an altitude below the ZWL, where the shear layer first occurs.

(3) Because the observations of the horseshoe-shaped vortices are such an important result of this study, Figures 10 and 11 show their development in some detail. Both Figure 10, with 9 panels, and Figure 11, with 15 panels, use the image-processing approach described earlier, where a fixed earlier image is used to subtract out most of the background. This has the advantage of retaining some aspect of the primary MWs (which changes in intensity as a function of time and thus are not completely subtracted out) and also bringing out the smaller-amplitude turbulent features. The panels are separated by 22 s and the figures cover the period from 233538 to 234417 UT.

Three interesting aspects of the small-scale structure are illustrated in these figures and are highlighted.

The top red arrow at 234013 UT in Figure 11 is a circular feature, which, when observed in the movie appears as almost a 3-D cylinder due to its motion. If that feature is followed backward in time in Figure 10, it is present between 233750 and 233834 UT as highlighted by red arrows. Before that, it seems to be part of a horseshoe

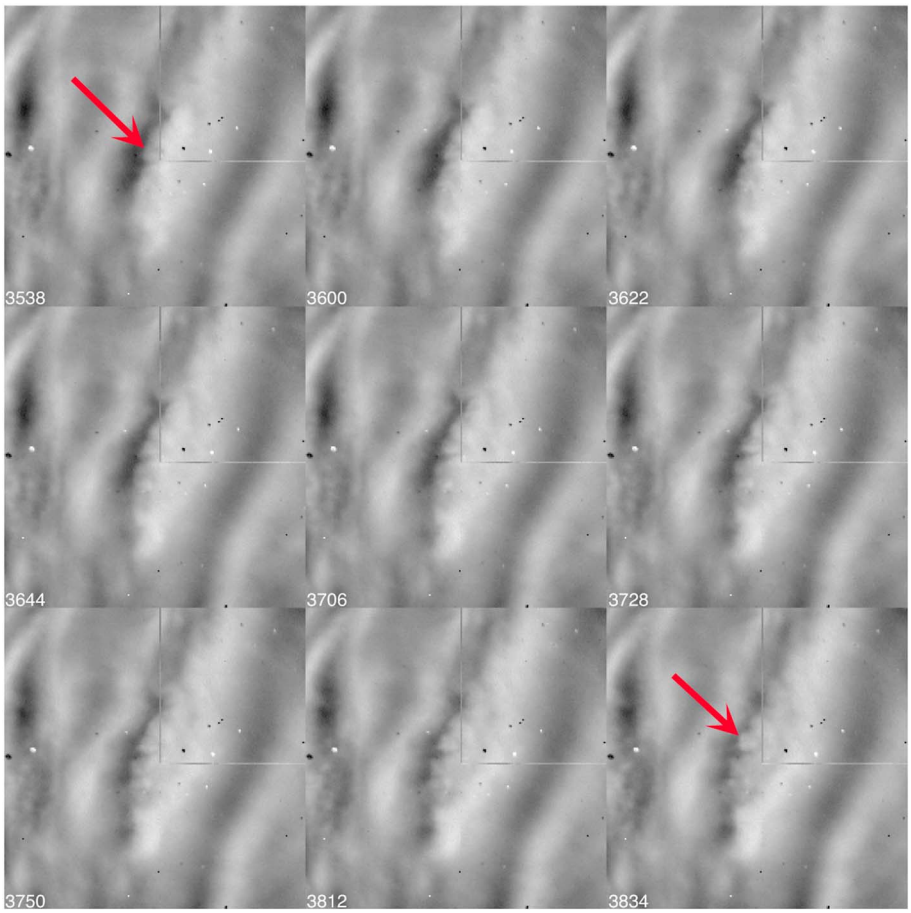

Figure 10. Similar to Figure 8 except that each image has a fixed time image (at 231219 UT) subtracted from it as described in the text. The period covered is from 233538 to 233834 UT with panels separated by 22 s.

vortex that forms around 233728. Before that, as indicated by the red arrow at 233538 UT in Figure 10, it is an isolated feature. The images/movie suggest that the first sign of this vortex/cylinder is close to 233300 UT. The feature appears to be dissipated by 234427 UT, suggesting a lifetime of around 11 min or nominally two T_b. The size of the feature is around 5 km.

From about 233900 to 234300 UT, easily seen in the movie but with a little more difficulty in Figure 11, this cylindrical feature seems to accelerate to a velocity of almost 50 m/s. The motion of this feature is different than the nominal motion of many of the instability structures which move at lower velocities, closer to 30 to 40 m/s.

The lower red arrow at 234013 UT in Figure 11 points to another horseshoe shaped vortex, with its open side aligned perpendicular to the wind. This feature seems to form just before 233900, and lasts until just before 234400 UT. Around 234200 UT the vortex rotates, and the open side then points west. This vortex also moves at a higher speed with the motion of the cylinder.

(4) Figure 12 shows five 1 min difference panels (the same mode as used in Figure 9), at about 1 min and 18 s intervals, from 000647 to 001158 UT on 9 July. These panels highlight the formation of two large-amplitude KHI phasefronts, which are fully formed in the last panel. The highlighted arrows indicate the positions of the KHI primary and secondary phase fronts.

The red arrow in the last panel points to the primary phase fronts. The length of the arrow is the horizontal wavelength of the primary KHI. Following these phase fronts back in time to the first panel shows their partial development at that time. Note that these phase fronts are parallel to the MW phase fronts.

The blue arrows in the last panel point to thin short lines which appear densely packed and are perpendicular to the KHI primary phase fronts. The second blue arrow shows that some of these lines extend between

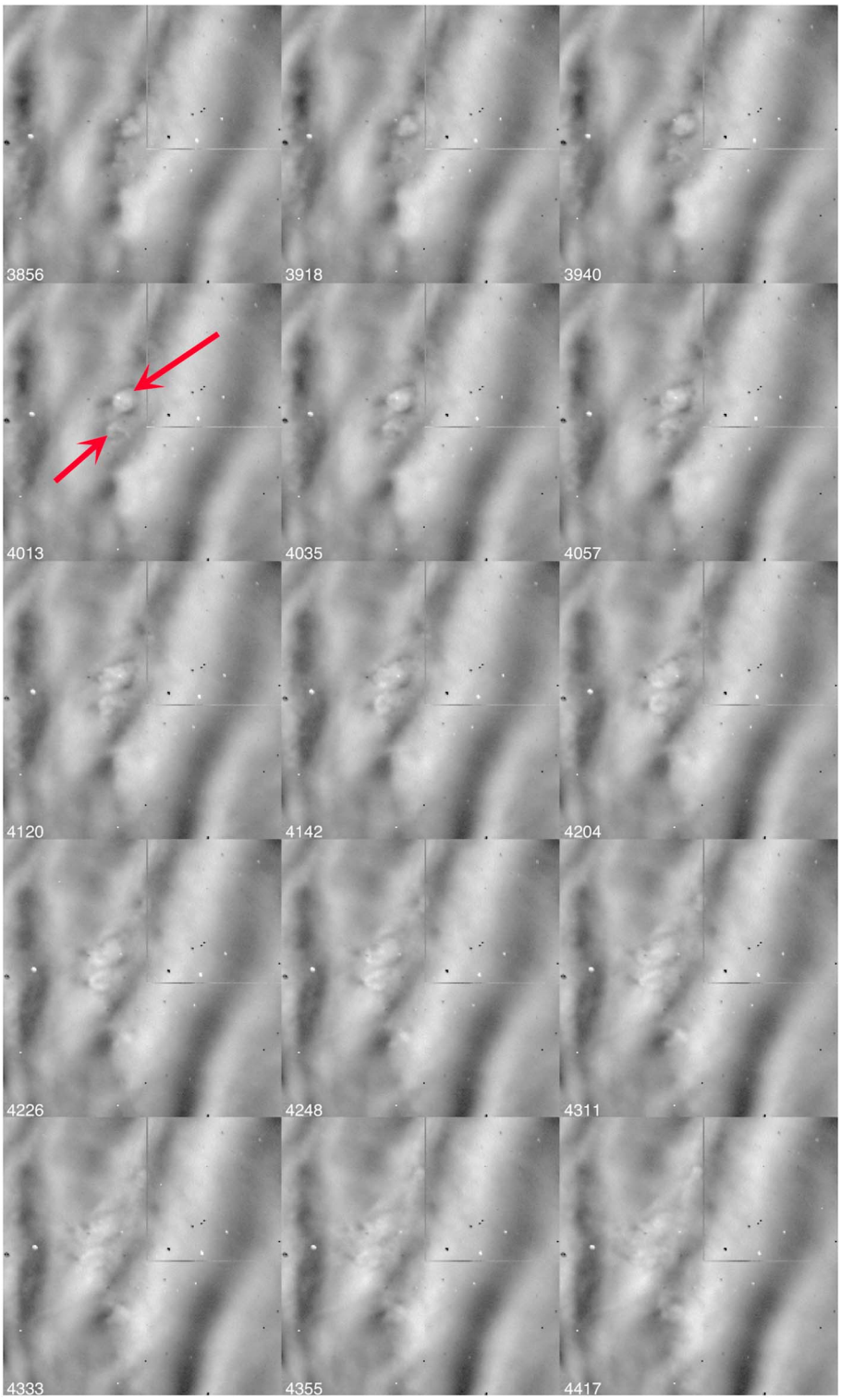

Figure 11. Similar to Figure 10 but for 233856 to 234417 UT.

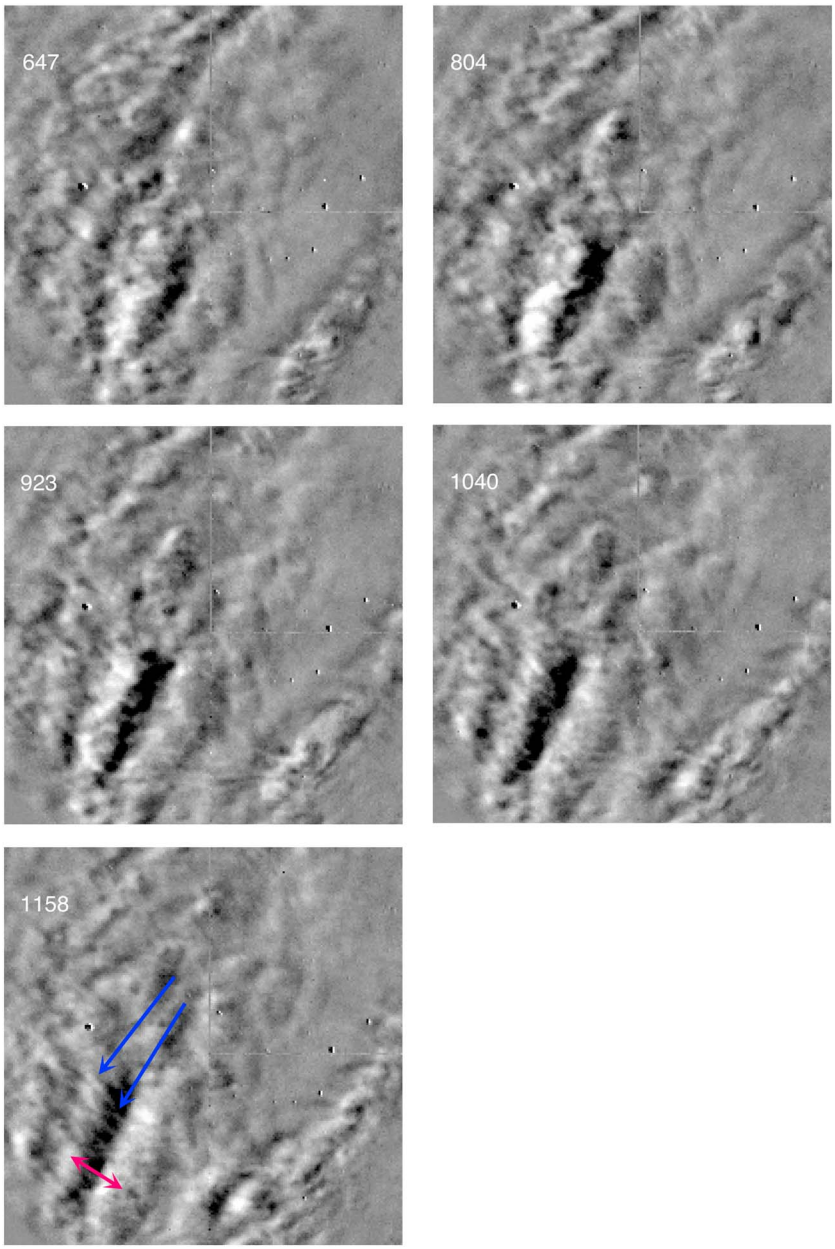

Figure 12. Same difference mode as Figure 9 but with five panels from 000647 UT to 001158 UT on 9 July.

the primary phase fronts. These are secondary instabilities (perpendicular structures to the primary phase fronts) which have been discussed in previous publications (see Fritts, Wan, et al., 2014 and Hecht et al., 2014 for more discussion). These secondary features appear to become well-formed after 001000 UT.

(5) Figure 13 shows this KHI in more detail, with an image at 001326 UT. The ratio of primary to secondary wavelengths is between 4 and 5, and this will be used below to infer a turbulent kinematic viscosity. One interesting aspect of the formation of the KHIs is that they form well after the production of the initial horseshoe-shaped vortices and appear to have no obvious connection with those structures.

4. Discussion

4.1. Overview of Model Simulations

Floquet or optimal perturbation theory can provide guidance for initial instabilities of AGWs in idealized and more realistic environments (e.g., Achatz, 2005, 2007; Lombard & Riley, 1996). Initial optimal perturbations

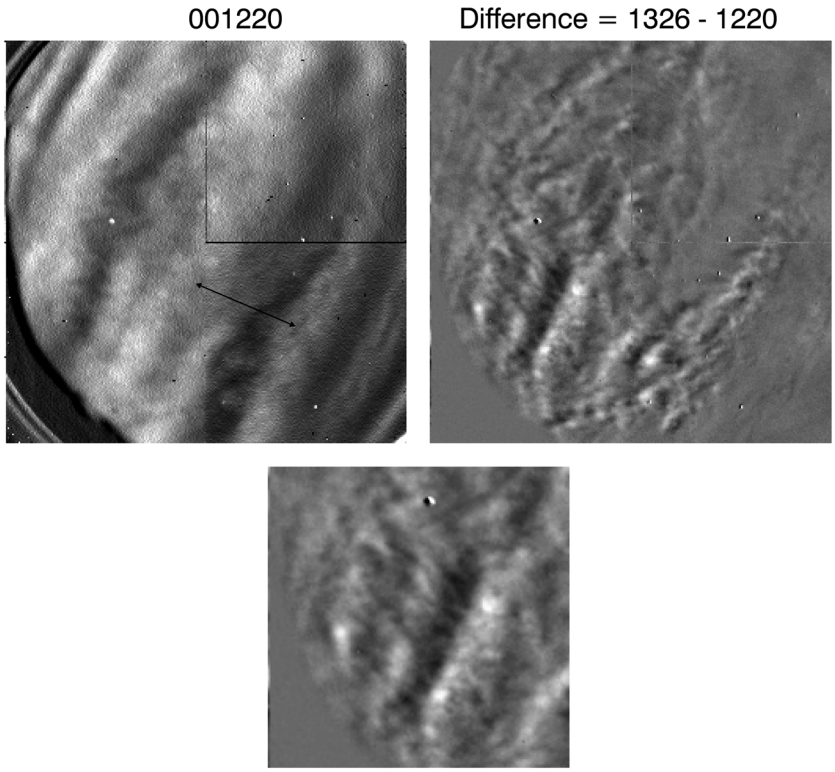

Figure 13. (top left) Raw flatfielded image at 001220 UT on 9 July. The detector has four 128 × 128 quadrants that make up the 256 × 256 image. The lines that separate the upper right quadrant are seen in this image and are due to the readout of this image. (top right) The difference between the two images at 001326 and 001220 UT. (bottom) An enlargement of the lower left quadrant.

arise throughout the AGW phase structure, but those that achieve finite amplitude occur preferentially between the phase of weakest N^2 and the sheared phase above (Fritts et al., 2009b). Their evolution, and the strong vortex dynamics driving turbulence thereafter, require a DNS description. Similar guidance on initial secondary instabilities in finite-amplitude KH billows correctly anticipates the instability scales that drive the evolution to turbulence in these flows (Klaassen & Peltier, 1991).

In the case of AGW breakdown, predictions of instability structures have been confirmed in applications to PMC observations from the ground and the stratosphere, but without detailed knowledge of the AGW environmental shear and stability (Fritts et al., 2017; Miller et al., 2015). Below, we employ the DNS results shown in Figure 14 in the interpretation of the small-scale AGW instability features described above.

The observations in this study show MW breaking occurring early in the MW evolution due to wave-induced instabilities, and large-amplitude KHIs occurring later due to apparent MW modulation of background shears, as discussed above. The instability dynamics driven by these MW environments are discussed below and compared with DNS of similar flows.

We note though that there is one particular aspect of past and very recent DNS that are observed in the present set of observations. Specifically, the following section shows that DNS do predict the presence of the horseshoe-shaped instabilities seen in both idealized AGW breaking and multiscale environments, and in these imaging data.

4.2. Evolution of the Vortex Ring Features Compared With DNS

One of the key characteristics observed in these airglow images is the presence of horseshoe-shaped vortex rings. Horseshoe/Hairpin vortices have long been recognized as an important feature in the early evolution of turbulent flows near the boundary layer (see, e.g., Hon & Walker, 1991; Singer & Joslin, 1994; Theodorsen, 1952, and references therein). Certainly in these MW images vortex rings appear to form early in the MW breakdown process. However, while the airglow images in this present study are obviously not from the boundary layer, this study and parallel investigations show that vortices occur frequently as a component of gravity wave

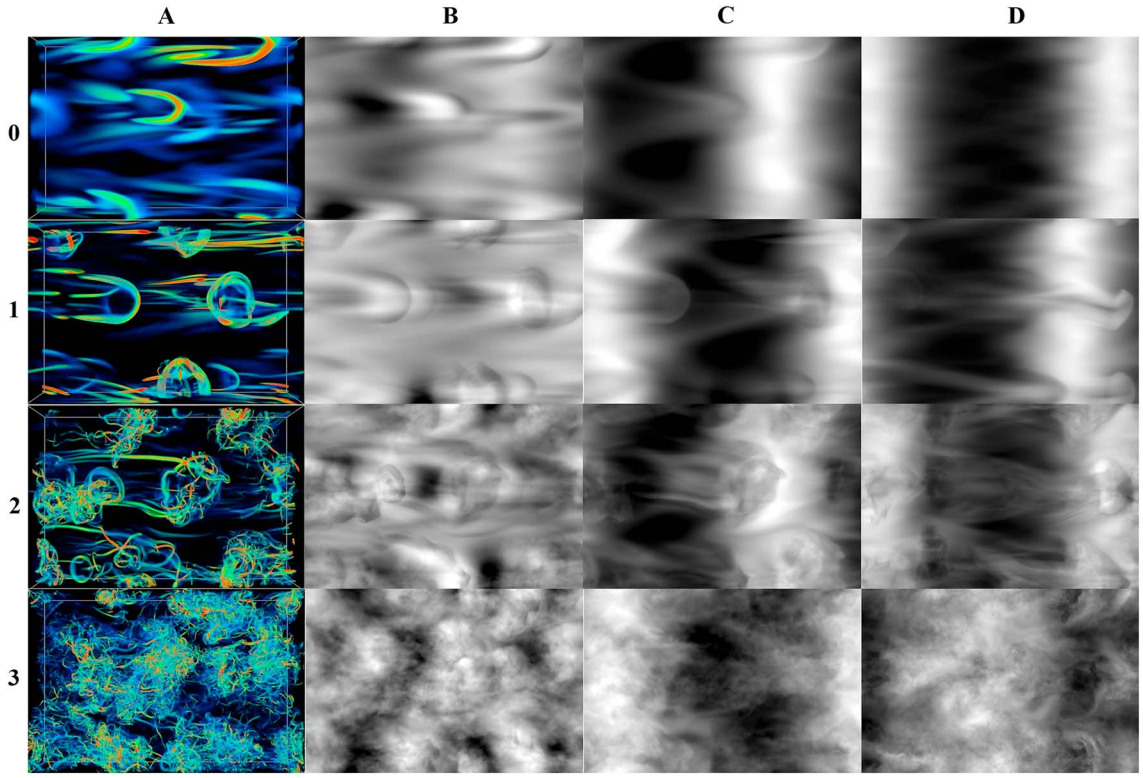

Figure 14. (column A) A DNS of AGW breaking dynamics for $a = |u'/c| = 0.9$ visualized in λ_2 (yellow/red is strong rotation, see text for details). From top to bottom, images are at intervals of 1 T_b. The AGW is propagating from left to right and viewed from below. (columns B and C) Simulated OH brightness are for the DNS fields in Figure 14 (column A), and initial Gaussian OH profiles having widths of 0.7 and 0.3 λ_z at altitudes revealing dynamics similar to those observed. (column D) Similar simulated OH images for an airglow layer having a width of 0.3 λ_z in a DNS of AGW breaking for $a = 1.1$.

instability dynamics in the mesopause region (see, e.g., Figure 7 in Fritts et al., 2017, and the discussion at the end of this subsection).

Since the 1990s a number of DNS have been performed addressing gravity wave breakdown in the UMLT. For this work two of the published studies are especially relevant, and remarkably, they show features that are quite similar in form and evolution to what we observe (Fritts et al., 1999, 2009b). These DNS were performed in an idealized environment with no mean shear and uniform N^2. AGW amplitudes of $a = |u'/c| = 0.9$ and 1.1 were chosen to explore instability dynamics above and below nominal AGW overturning (i.e., $a = 1$ and minimum $N^2 = 0$). An AGW intrinsic frequency of $\omega_i = N/3.2$ was assumed in each case. An $Re = \lambda_z^2/\nu T_b = 10,000$ was assumed in order to ensure instability and turbulence dynamics representative of MLT altitudes. Importantly, as shown by Fritts et al. (2009a, 2009b), instability dynamics in the two cases are very similar, though somewhat slower to evolve for $a = 0.9$. These results confirm clearly, for these AGW parameters at least, what has been shown by previous analyses of instabilities of AGWs (e.g., Achatz, 2005, 2007; Lombard & Riley, 1996; Sonmor & Klaassen, 1997); that is, there are no specific thresholds for AGW instabilities and turbulence to arise.

Results of these DNS of relevance to our MW instability analysis here are shown in Figure 14 (column A). Shown are four volumetric views of λ_2, which quantifies the rotational character of the local vorticity field (see Jeong & Hussain, 1995 and Andreassen et al., 1998). These images span 3 T_b, and the transition from initial optimal perturbations to fully developed turbulence extending to much smaller scales. Initial optimal perturbations are slanted horizontally with respect to the streamwise direction (along the AGW propagation). As these initial vortex structures intensify, they interact with an intensifying spanwise vorticity sheet below that links adjacent vortices having the opposite streamwise vorticity to form horseshoe-shaped vortices (see first panel of Figure 14, column A). The horseshoe vortices induce strong local downward motions that quickly evolve to vortex rings (second panel of Figure 14, column A), which themselves exhibit strong vorticity dynamics and a rapid cascade to turbulence thereafter (see Andreassen et al., 1998 and Fritts et al., 1998 for additional details).

The implications of these dynamics for OH airglow imaging are explored as described in section 2.4 above. We assume that OH airglow brightness is approximately conserved following air motions on the rapid time scales of AGW instability and turbulence dynamics. This allows a Gaussian OH layer to be specified in terms of potential temperature, which is approximately conserved throughout the DNS, as described by Fritts, Wan et al., (2014). OH images are shown, in columns B and C, respectively, corresponding to the vorticity images at column A, for assumed Gaussian widths of 0.7 and 0.3 λ_z and at altitudes chosen to provide comparisons with the observed OH images. Column D provides similar simulated OH images for an AGW having $a = 1.1$ and an OH layer depth of 0.3 λ_z. All three OH image sequences capture various aspects of the vorticity dynamics shown at the left, but the details revealed depend on the location of the OH layer in altitude and the time viewed. For example, the right sequence shows an earlier stage of horseshoe vortex formation and a later stage of vortex ring evolution because of the more rapid evolution of the DNS for $a = 1.1$. This seems to correspond quite well to what is observed. Although the airglow features actually observed seem more well defined than the images in Columns B and C suggest, this difference is most likely due to the choice of where the GW is placed in the airglow layer. Similarly, while the observed approximate 1 to 2 T_b lifetime of the vortices is somewhat less than the modeled 2 to 3 T_b value, this difference may be partly due to an incomplete knowledge of N at the location of these features.

Another result of the modeling relates to the observations shown in Movie S1 in the supporting information file. This shows that the initial velocity of the horseshoe vortices appears to be confined close to the center of the image for the first 10 min or so after the initial formation. Then there is a sudden acceleration. These observations are consistent with the production of turbulent features in a breaking MW. For example, consider that in a breaking wave u' is equal to $c - \bar{u}_k$ (Orlanski & Bryan, 1969), where u' is the wave-induced wind amplitude and $\bar{u}_k$ is the mean wind in the direction of the wave vector k. Then, for a MW where c is zero, u' is equal to $-\bar{u}_k$. In such a wave, initial instability structures (e.g., emerging horseshoe vortices) arise in the mountain wave phase propagating upstream (upward and westward) such that their motion appears close to stationary, perpendicular to the mountain wave phase fronts, in a ground-based frame of reference. As these initial instabilities cascade to vortex rings and turbulence over ≈0.5 of a mountain wave period, they are advected into the opposite phase of the mountain wave, (see, e.g., Fritts et al., 2009a). Additionally, the mountain wave amplitude decreases strongly as the instabilities and turbulence arise. Together, these effects cause the instability and turbulence features to advect eastward approximately with the mean wind thereafter, consistent with the observations. Note though, that during the initial advection into the opposite wave phase, the features could achieve a velocity above the mean wind, depending on how long it takes for the wave amplitude to decay at that altitude. Thus, some of the apparent initial acceleration of the vortices seen in the images may be due to this effect.

4.3. KHI Observations

Shortly after 0 UT on 9 July large-amplitude/horizontal wavelength KHIs were imaged moving between 30 and 40 m/s eastward. Given a horizontal wavelength of the primary KHI waves, λ_p, of around 12 km implies an unstable shear layer of around 1.66 km based on the formula from Fritts and Wan et al. (2014), $h = 0.436 * \lambda_p/(2. * \pi)$ where h is half the depth of the shear layer. This layer depth is quite large and given the discussion in section 3.5 it seems unlikely that these KHIs are forming within the large background shear present from 83 to 84 km shown in Figure 6. Furthermore, given that the motion of the KHIs are in the eastward direction with a velocity above 30 m/s suggests that they are occurring around 82 to 83 km altitude, below the shear and ZWL which are above 83 km.

One way these could form is a combination of (a) the background wind shear and temperature gradient, both of which are low in the altitude region below 83 km, with (b) the wave-induced shear and lapse rate. As discussed earlier, for an AGW the wave-induced temperature lapse and shear depend on the amplitude and vertical wavelength of the wave. Here we assume the wind and temperature waves are in quadrature and that the wind amplitude, u′ can be approximated by gA/N where A is the fractional temperature fluctuation following Hecht et al. (2001) and Walterscheid and Schubert (1990). Figure 15 presents calculations of Ri for this model where a 14 K amplitude wave was assumed, based on section 3.5, while the background shear was taken to be low, 5 m/s/km, a value representative of this period based on Figure 6.

The results are plotted as a function of background wind and lapse rate. A dashed horizontal line is shown for the Ri value of 0.25, which classically bounds the formation regions for KHIs instabilities, although this boundary should not be considered rigid for the formation of any instability structure (Walterscheid et al., 2013).

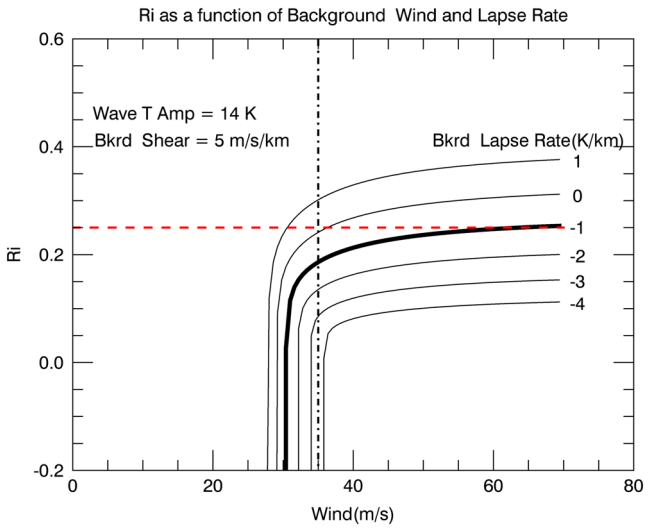

Figure 15. Plots of *Ri* versus (a) the background wind in the direction of the wave and (b) the background d*T*/d*z* (shown in black). A 14 K wave amplitude and a 5 m/s/km background shear are assumed for these calculations. The colored dashed line shows the classical *Ri* boundary for the formation of KHI. The vertical dash-dotted line highlights the nominal background wind of 35 m/s. The heavy black line highlights a d*t*/d*z* of −1 K/km. See text for more discussion.

Since, as inferred from the SABER profiles in Figure 5, the lapse rate may be low in this altitude region, a value of −1 K/km is highlighted as a thick line. Note that for all lapse rates, wind magnitudes below a certain value cause N^2 to rapidly fall below zero indicating a potentially convectively unstable region.

The −1 K/km line in particular addresses the question of why KHIs may not have been present earlier. Figure 6 shows that the winds below 90 km from 22 to 23 UT on 8 July were quite high, reaching nearly 70 m/s at 83 km. The results of Figure 15 suggest the atmosphere would be stable, in a classical sense, for winds above 50 m/s providing the background shear and lapse rate are low. However, as the ZWL decreased in altitude, the winds in the OHVER layer decreased. As these winds decrease in magnitude, Figure 15 plausibly suggests that, even for low shears and lapse rates in the background, this large-amplitude mountain wave would cause the atmosphere to go dynamically unstable allowing KHI formation.

The thickness of the unstable region can also be predicted using the vertical wavelength and temperature amplitude of the wave. For 35 m/s background winds, a background lapse rate of −0.5 K/km, and a 5 m/s/km background shear, all appropriate for the altitude region around 82 to 83 km, an unstable layer with a mean *Ri* of 0.22 will form about 1.5 km thick due to the combined background and wave-induced winds and temperatures. This layer thickness would be close to what is observed. The mean shear in this layer due to the MW is about 30 m/s/km, and the total shear is 35 m/s/km.

While this analysis is not confined to a specific altitude or wind, it does strongly suggest that for the conditions seen in this event, KHI formation is quite likely at altitudes within 1 to 2 km below the ZWL.

4.4. Background Turbulent Kinematic Viscosity

As Guo et al. (2017) have recently noted, measurements of the atmospheric diffusion is relatively challenging, and there have been few locations where such data are available. Even scarcer are the availability of such data during instability events (see, e.g., Bishop et al., 2004). As discussed in Hecht et al. (2014) the background turbulent kinematic viscosity can often be estimated from the properties of observed KHIs. In particular, ν, can be derived from *Re* and from a combination in the unstable shear layer of the half-velocity and half shear depth. *Re* can be inferred using DNS model runs found in Fritts, Wan et al. (2014), which estimate *Re* as a function of the ratio of the primary to secondary wavelengths of an observed KHI. For the KHI discussed here, that are present around 001000 UT on 9 July, the primary KHI horizontal wavelength is 12 km, and the primary to secondary wavelength ratio is between 4 and 5. Thus, *Re* is estimated from Fritts, Wan et al., (2014) to be around 800. This is consistent with older model estimates of *Re* as a function of this ratio (see, e.g., Klaassen & Peltier, 1985a, 1985b, 1991). The half-velocity (U) is taken as around 26 m/s, over this distance, based on the mean shear. Given these numbers, ν is 25 m^2/s which is much higher than the nominal molecular value close to 1 m^2/s, at 83 km, in a standard atmosphere (see, e.g., the references in Minzner, 1977). Even a combined error of a factor of 2 in the value of U/Re still leaves this measurement larger than the molecular value. This value is also higher than the nominal value of 5 to 10 m^2/s for the eddy diffusion used in WACCM (Whole Atmosphere Community Climate Model) (Smith, 2012). We note that, recently, Guo et al. (2017) have reported results for the thermal diffusivity from data at ALO, also higher than those found by Smith (2012). Those data, however, are an average of many nights and are at a higher altitude than in this data set, and thus cannot directly be compared to the present results. Thus, at the time the KHIs appeared the background atmosphere was turbulent, consistent with the nearly 1 h dissipation of the MWs into turbulent structures that preceded the KHI formation.

5. Conclusions

The following are the main results of this study.

1. Mountain waves (MWs) were observed from 2240 UT on 8 July 2012 to after 0200 UT on 9 July 2012.

2. Turbulence, presumably associated with convective instabilities and MW breakdown, and Kelvin Helmholtz Instability (KHI) formation were initiated around 2310 to 2320 UT on 8 July 2012. These initiations were caused by the zero wind line (ZWL) and associated wind shear descending into the airglow layer.
3. MW breakdown and its associated turbulence was probably triggered by the temperature gradient in the MW which, when added to the background lapse rate, caused the MW to go unstable, initially at a single location.
4. MW dissipation in the OH layer occurred continuously after the initial observations until after 0230 UT, as the ZWL passed through and below the OH volume emission region.
5. Horseshoe-shaped vortex rings were observed and lasted about 1 to 2 T_b. These features appear to be a common feature in the transition to turbulence near boundary layers. It is noteworthy that they are features of both DNS of gravity wave breakdown in the OH airglow layer and of OH airglow imaging observations of MW breakdown.
6. Large-amplitude KHIs appeared after the vortex rings dissipated, and their formation was due to the reduced background wind velocities in the OHVER, below the large shear, as the ZWL descended. The ratio of the primary to secondary KHI wavelengths was between 4 and 5, while the primary KHI horizontal wavelength was 12 km. These KHI parameters, the inferred wave-induced and background shear and temperature gradient, and previous DNS allowed an estimate of the background turbulent kinematic viscosity. This viscosity was around 25 m^2/s, a value high than is found in a standard atmosphere or in WACCM near 83 km altitude.

Appendix A

The purpose of this appendix is to show how the MW amplitude can be recovered from the change in the observed MW phase cancellation as the ZWL descends through the airglow layer. Below the descending ZWL a constant wind shear layer of 30 m/s and a nominal 0 m/s MW phase speed are assumed. For this analysis the MW vertical wavelength is taken as 14 km given nominal velocities of 35 m/s for the velocity of the instability features, which reflect the wind below the ZWL, a background temperature of 210 K, a background lapse rate of −2 K/km, and a MW horizontal wavelength of approximately 35 km.

As the ZWL descends, the MW approaches a critical level, where the wind velocity is 0 m/s, at altitudes within the OH airglow emission layer. The behavior of a wave approaching such a critical level has been the subject of numerous studies (Booker & Bretherton, 1967; Bretherton, 1966; Fritts, 1979; Fritts & Dunkerton, 1984; Gardner & Taylor, 1998; Hazel, 1967; Hickey et al., 1998; Hines, 1974; Pitteway & Hines, 1963; Vadas & Fritts, 2005).

These studies show that the critical layer is often a very effective barrier to wave propagation. While there are some studies that show that waves can propagate in some form above this layer (e.g., Fritts, 1979; Hickey et al., 1998), the lack of MWs in the BU greenline image data for the present set of observations suggests that the ZWL acted as a descending barrier, above which the MW could not propagate in its original form.

Based on the discussion in section 3.5 and the above references, for a constant mean wind shear below the ZWL, the MW vertical wavelength, on its approach to the critical layer altitude, decreases directly in proportion to the distance to the ZWL, assuming a constant N. At the same time the MW horizontal wind/temperature amplitude increases as the inverse of the square root of that distance.

The result of these changes in the MW properties suggest two likely effects that can cause significant reduction in the MW amplitude on its approach to the critical level altitude. If the MW amplitude is small and the kinematic viscosity is large, the MW will undergo viscous dissipation due mainly to the reduction in the MW vertical wavelength. However, based on Pitteway and Hines (1963) and Hazel (1967), and for the modest background kinematic viscosity and vertical wavelength inferred in this study, this would only occur within about 100 m of the ZWL.

If the MW amplitude is large and the background kinematic viscosity is small, then N^2 is likely to approach zero, implying overturning, well before reaching the viscous dissipation region. Based on the criteria discussed in section 1, MW breakdown and instability formation are likely to occur. The appearance of instability-like features in the image observations, at one location of the MW phase, suggests that MW breakdown is occurring, due to the steep temperature gradient in one phase of the MW combined with the background temperature gradient.

Given that as the ZWL descends into the airglow emission layer the MW is not present above the ZWL, a variation of the MW phase cancellation occurs in the airglow layer. Thus, as the ZWL descends, the amplitude of the MW as seen from the ground should vary. Therefore, the MTM OH temperature variations shown in Figure 7 can be used to determine the actual amplitude of the wave if the rate of the descent of the ZWL and the shape of the OH VER are known.

To account for the descent of the ZWL in this analysis, a shear layer was adopted that (a) reduced a 35 m/s wind, in the direction of the MW, to zero over 1 km, and (b) descended at 4 km/h. Increasing this width of the layer to 2 km had little effect with respect to the conclusions of this analysis. Thus, the wind was taken to be constant from where the OH layer begins (taken to be 78 km) until the descending shear layer was encountered, and then within 1 km the wind went linearly to zero. For the phases of the MW that existed in the shear layer, as the wind velocity decreased, both the vertical wavelength decreased and the amplitude increased as noted above.

To account for the effect of phase cancellation within the OHVER shape, a 14 km vertical wavelength was adopted. Given this wavelength, and for three different maximum temperature amplitudes, 4 K, 9 K, and 14 K, the wave was convolved with the OHVER observed by SABER, at 0112 UT as shown in Figure 5, for 14 different altitudes for the position of the maximum wave amplitude.

To make comparisons with the MTM results in Figure 7 the following approach was adopted. First, a 14 km vertical wavelength temperature wave was convolved with the OHVER until the shear layer was reached. Then the wave amplitude and wavelength were modified every 10 m and convolved with the OHVER for either (a) an additional 100 m, as would be appropriate for overturning rapidly forming, or for (b) an additional 950 m, which is at a distance 50 m below the ZWL, appropriate for viscous dissipation to occur. These two cases represent realistic limits for modeling the phase cancellation effects. To compare with the MTM data, this integration was performed every 0.25 h, and since the altitude of the shear layer was descending at a rate of 4 km/h, this gives 1 km vertical steps.

Figure 7 shows some of the apparent fractional fluctuation results for the 950 m (dashed line) and 100 m (dash-dotted line) integration limits, and the measured data. These results were chosen to best match the data. For the dashed line results the wave phase giving the maximum temperature amplitude was centered at 84 km. While the time variations of all three amplitudes resemble the data, the 4 and 9 K amplitudes produce too small a maximum.

An amplitude of 14 K produces a predicted ground observation of the fractional temperature fluctuation that best matches the variation seen by the MTM. The dash-dotted line shows that if the integration only continues through the first 100 m of the shear layer, the modeled match with the MTM is still reasonable. For this case, the peak amplitude is 1 km lower, at 83 km.

In either case, since such a large-amplitude wave probably does dissipate due to the formation of instabilities shortly after entering the shear layer, it is likely that viscous dissipation near the ZWL is not a significant process for these observations. In fact, the observed velocities near 30 to 40 m/s of the instability features in the airglow images suggest that this is a realistic model.

Acknowledgments
We thank Steve Heathcote and the staff at the Cerro Tololo Inter-American Observatory and especially at SOAR on Cerro Pachon for providing support for all the instrumentation and for the operations at the Andes Lidar Observatory. Support for J. H. H., L. J. G., R. J. R., and R. L. W. was provided by NSF grants AGS-1110206 and AGS-1450660 and by the Aerospace Corporation's SERPA program. Support for D. C. F. was provided by NSF grants AGS-1136269, AGS-1445783, and AGS-1149633. P. D. P. and M. J. T. were supported by NSF grant AGS-1110215. Support for L. W. was provided by NSF grants AGS-1510354 and AGS-1632772. S. J. F. was supported by NSF grant 1110334. Support for S. S. was provided by NSF grant AGS-0940148. As noted in the text the images/movie contain some of the data used for the analysis in this paper. Any additional data can be obtained by contacting the lead author.

References

Achatz, U. (2005). On the role of optimal perturbations in the instability of monochromatic gravity waves. *Physics of Fluids*, *17*, 94107. https://doi.org/10.1063/1.2X00000

Achatz, U. (2007). The primary nonlinear dynamics of modal and nonmodal perturbations of monochromatic inertia-gravity waves. *Journal of the Atmospheric Sciences*, *64*, 74–95.

Alexander, M. J., & Teitelbaum, H. (2011). Three-dimensional properties of Andes Mountain waves observed by satellite: A case study. *Journal of Geophysical Research*, *116*, D23110. https://doi.org/10.1029/2011JD016151

Andreassen, O., Hvidsten, P. O., Fritts, D. C., & Arendt, S. (1998). Vorticity dynamics in a breaking internal gravity wave. Part 1. Initial instability evolution. *Journal of Fluid Mechanics*, *367*, 27–46.

Andreassen, O., Wasberg, C. E., Fritts, D. C., & Isler, J. R. (1994). Gravity wave breaking in two and three dimensions: 1. Model description and comparison of two-dimensional evolutions. *Journal of Geophysical Research*, *99*, 8095–8108.

Baumgarten, G., & Fritts, D. C. (2014). Quantifying Kelvin-Helmholtz instability dynamics observed in noctilucent clouds: 1. Methods and observations. *Journal of Geophysical Research: Atmospheres*, *119*, 9324–9337. https://doi.org/10.1002/2014JD021832

Bishop, R. L., Larsen, M. F., Hecht, J. H., Liu, A. Z., & Gardner, C. S. (2004). TOMEX: Mesospheric and lower thermospheric diffusivities and instability layers. *Journal of Geophysical Research*, *109*, D02S03. https://doi.org/10.1029/2002JD003079

Booker, J. R., & Bretherton, F. P. (1967). The critical layer for internal gravity waves in a shear flow. *Journal of Fluid Mechanics*, *27*, 513–539.

Bretherton, F. P. (1966). The propagation of groups of internal gravity waves in a shear flow. *Quarterly Journal of the Royal Meteorological Society*, *92*, 466–480.

Cai, X., Yuan, T., Zhao, Y., Pautet, P.-D., Taylor, M. J., & Pendleton, Jr. W. R. (2014). A coordinated investigation of the gravity wave breaking and the associated dynamical instability by a Na lidar and an advanced mesosphere temperature mapper over Logan, UT (41.7°N 111.8°W). *Journal of Geophysical Research: Space Physics*, *119*, 6852–6864. https://doi.org/10.1002/2014JA020131

Drazin, P. G. (1958). The stability of a shear layer in an unbounded heterogeneous inviscid fluid. *Journal of Fluid Mechanics*, *4*(2), 214–224. https://doi.org/10.1017/S0022112058X00000

Franke, S. J., Chu, X., Liu, A. Z., & Hocking, W. K. (2005). Comparison of meteor radar and Na Doppler lidar measurements of winds in the mesopause region above Maui, Hawaii. *Journal of Geophysical Research*, *110*, D09S02. https://doi.org/10.1029/2003JD004486

Fritts, D., & Dunkerton, T. J. (1984). A quasi-linear study of gravity-wave saturation and self-acceleration. *Journal of the Atmospheric Sciences*, *41*(22), 3272–3289.

Fritts, D. C. (1979). The excitation of radiating waves and Kelvin-Helmholtz instabilities by the gravity wave-critical level interaction. *Journal of the Atmospheric Sciences*, *36*, 12–23. https://doi.org/10.1175/1520-0469(1979)036<0012:TEORWA>2.0.CO;2

Fritts, D. C., & Alexander, M. J. (2003). Gravity wave dynamics and effects in the middle atmosphere. *Reviews of Geophysics*, *41*(1), 1003. https://doi.org/10.1029/2001RG000106

Fritts, D. C., Arendt, S., & Andreassen, O. (1998). Vorticity dynamics in a breaking internal gravity wave. Part 2. Vortex interactions and transition to turbulence. *Journal of Fluid Mechanics*, *367*, 47–65.

Fritts, D. C., Arendt, S., & Andreassen, Ø (1999). The vorticity dynamics of instability and turbulence in a breaking internal gravity wave. *Earth, Planets and Space*, *51*, 457–473. https://doi.org/10.1186/BF03353208

Fritts, D. C., Baumgarten, G., Wan, K., Werne, J., & Lund, T. (2014). Quantifying Kelvin-Helmholtz instability dynamics observed in noctilucent clouds: 2. Modeling and interpretation of observations. *Journal of Geophysical Research: Atmospheres*, *119*, 9359–9375. https://doi.org/10.1002/2014JD021833

Fritts, D. C., Bizon, C., Werne, J. A., & Meyer, C. K. (2003). Layering accompanying turbulence generation due to shear instability and gravity wave breaking. *Journal of Geophysical Research*, *108*(D8), 8452. https://doi.org/10.1029/2002JD002406

Fritts, D. C., Garten, J. F., & Andreassen, O. (1996). Wave breaking and transition to turbulence in stratified shear flows. *Journal of the Atmospheric Sciences*, *53*, 1057–1085.

Fritts, D. C., Isler, J. R., & Andreassen, Ø. (1994). Gravity wave breaking in two and three dimensions: 2. Three-dimensional evolution and instability structure. *Journal of Geophysical Research*, *99*(D4), 8109–8123. https://doi.org/10.1029/93JD03436

Fritts, D. C., Isler, J. R., Hecht, J. H., Walterscheid, R. L., & Andreassen, Ø. (1997). Wave breaking signatures in sodium densities and OH nightglow: 2. Simulation of wave and instability structures. *Journal of Geophysical Research*, *102*(D6), 6669–6684. https://doi.org/10.1029/96JD01902

Fritts, D. C., Isler, J. R., Thomas, G. E., & Andreassen, O. (1993). Wave breaking signatures in noctilucent clouds. *Geophysical Research Letters*, *20*(19), 2039–2042. https://doi.org/10.1029/93GL01982

Fritts, D. C., Palmer, T. L., Andreassen, O., & Lie, I. (1996). Evolution and breakdown of Kelvin-Helmoholtz billows in stratified compressible flows. Part I: Comparison of two- and three-dimensional flows. *Journal of the Atmospheric Sciences*, *53*, 3173–3191.

Fritts, D. C., Wan, K., Franke, P., & Lund, T. (2012). Computation of clear-air radar backscatter from numerical simulations of turbulence: 3. Off-zenith measurements and biases throughout the lifecycle of a Kelvin-Helmholtz instability. *Journal of Geophysical Research*, *117*, D17101. https://doi.org/10.1029/2011JD017179

Fritts, D. C., Wan, K., Werne, J., Lund, T., & Hecht, J. H. (2014). Modeling the implications of Kelvin-Helmholtz instability dynamics for airglow observations. *Journal of Geophysical Research: Atmospheres*, *119*, 8858–8871. https://doi.org/10.1002/2014JD021737

Fritts, D. C., Wang, L., Baumgarten, G., Miller, A. D., Geller, M. A., Jones, G., … Vinokurov, J. (2017). High-resolution observations and modeling of turbulence sources, structures, and intensities in the upper mesosphere. *Journal of Atmospheric and Solar-Terrestrial Physics*, *162*, 57–78. https://doi.org/10.1016/j.jastp.2016.11.006

Fritts, D. C., Wang, L., Geller, M. A., Lawrence, D. A., Werne, J., & Balsey, B. B. (2016). Numerical modeling of multiscale dynamics at a high Reynolds number: Instabilities, turbulence, and an assessment of Ozmidov and Thorpe scales. *Journal of the Atmospheric Sciences*, *73*, 555–578. https://doi.org/10.1175/JAS-D-14-0343.1

Fritts, D. C., Wang, L., & Werne, J. (2013). Gravity wave fine structure interactions, Part 1: Influences of fine-structure form and orientation on flow evolution and instability. *Journal of the Atmospheric Sciences*, *70*, 3710–3734. https://doi.org/10.1175/JAS-D-13-055.1

Fritts, D. C., Wang, L., & Werne, J. (2009). Gravity wave fine structure interactions: A reservoir of small-scale and large-scale turbulence energy. *Geophysical Research Letters*, *36*, L19805. https://doi.org/10.1029/2009GL039501

Fritts, D. C., Wang, L., Werne, J., Lund, T., & Wan, K. (2009a). Gravity wave instability dynamics at high Reynolds numbers, 1: Wave field evolution at large amplitudes and high frequencies. *Journal of the Atmospheric Sciences*, *66*, 1126–1148. https://doi.org/10.1175/2008JAS2726.1

Fritts, D. C., Wang, L., Werne, J., Lund, T., & Wan, K. (2009b). Gravity wave instability dynamics at high Reynolds numbers, 2: Turbulence evolution, structure, and anisotropy. *Journal of the Atmospheric Sciences*, *66*, 1149–1171. https://doi.org/10.1175/2008JAS2727.1

Gardner, C. S., & Taylor, M. J. (1998). Observational limits for lidar, radar, and airglow imager measurements of gravity wave parameters. *Journal of Geophysical Research*, *103*(D6), 6427–6437. https://doi.org/10.1029/97JD03378

Guo, Y., Liu, A. Z., & Gardner, C. S. (2017). First Na lidar measurements of turbulence heat flux, thermal diffusivity, and energy dissipation rate in the mesopause region. *Geophysical Research Letters*, *44*, 5782–5790. https://doi.org/10.1002/2017GL073807

Hazel, P. (1967). The effect of viscosity and heat conduction on internal gravity waves at a critical level. *Journal of Fluid Mechanics*, *30*, 775–786.

Hecht, J. H. (2004). Instability layers and airglow imaging. *Reviews of Geophysics*, *42*, RG1001. https://doi.org/10.1029/2003RG000131

Hecht, J. H., Liu, A. Z., Bishop, R. L., Clemmons, J. H., Gardner, C. S., Larsen, M. F., … Walterscheid, R. L. (2004). An overview of observations of unstable layers during the Turbulent Oxygen Mixing Experiment (TOMEX). *Journal of Geophysical Research*, *109*, D02S01. https://doi.org/10.1029/2002JD003123

Hecht, J. H., Liu, A. Z., Walterscheid, R. L., Franke, S. J., Rudy, R. J., Taylor, M. J., & Pautet, P.-D. (2007). Characteristics of short-period wavelike features near 87 km altitude from airglow and lidar observations over Maui. *Journal of Geophysical Research*, *112*, D16101. https://doi.org/10.1029/2006JD008148

Hecht, J. H., Liu, A. Z., Walterscheid, R. L., & Rudy, R. J. (2005). Maui mesosphere and lower thermosphere (Maui MALT) observations of the evolution of Kelvin-Helmholtz billows formed near 86 km altitude. *Journal of Geophysical Research*, *110*, D09S10. https://doi.org/10.1029/2003JD003908

Hecht, J. H., Walterscheid, R. L., Fritts, D. C., Isler, J. R., Senft, D. C., Gardner, C. S., & Franke, S. J. (1997). Wave breaking signatures in OH airglow and sodium densities and temperatures: 1. Airglow imaging, Na lidar, and MF radar observations. *Journal of Geophysical Research*, *102*, 6655–6668. https://doi.org/10.1029/96JD02619

Hecht, J. H., Walterscheid, R. L., & Vincent, R. A. (2001). Airglow observations of dynamical (wind shear-induced) instabilities over Adelaide, Australia, associated with atmospheric gravity waves. *Journal of Geophysical Research*, *106*(D22), 28,189–28,197. https://doi.org/10.1029/2001JD000419

Hecht, J. H., Wan, K., Gelinas, L. J., Fritts, D. C., Walterscheid, R. L., Rudy, R. J., … Swenson, G. R. (2014). The life cycle of instability features measured from the Andes Lidar Observatory over Cerro Pachon on 24 March 2012. *Journal of Geophysical Research: Atmospheres*, *119*, 8872–8898. https://doi.org/10.1002/2014JD021726

Hickey, M. P., Taylor, M. J., Gardner, C. S., & Gibbons, C. R. (1998). Full-wave modeling of small-scale gravity waves using Airborne Lidar and Observations of the Hawaiian Airglow (ALOHA-93) O(1 S) images and coincident Na wind/temperature lidar measurements. *Journal of Geophysical Research*, *103*(D6), 6439–6453. https://doi.org/10.1029/97JD03373

Hines, C. O. (1974). Some consequences of gravity-wave critical layers in the upper atmosphere. In *The Upper Atmosphere in Motion*. Washington, DC: American Geophysical Union. https://doi.org/10.1029/GM018p0615

Hon, T. L., & Walker, J. D. A. (1991). Evolution of hairpin vortices in a shear flow. *Computers and Fluids*, *20*, 343–358.

Jeong, J., & Hussain, F. (1995). On the identification of a vortex. *Journal of Fluid Mechanics*, *285*, 69–94. https://doi.org/10.1017/S0022112095X00000

Jiang, J. H., Wu, D. L., & Eckermann, S. D. (2002). Upper Atmosphere Research Satellite (UARS) MLS observation of mountain waves over the Andes. *Journal of Geophysical Research*, *107*(D20), 8273. https://doi.org/10.1029/2002JD002091

Klaassen, G. P., & Peltier, W. R. (1985a). The evolution of finite amplitude Kelvin-Helmholtz billows in two spatial dimensions. *Journal of the Atmospheric Sciences*, *42*, 1321–1339.

Klaassen, G. P., & Peltier, W. R. (1985b). The onset of turbulence in finite amplitude Kelvin-Helmholtz billows. *Journal of Fluid Mechanics*, *155*, 1–35.

Klaassen, G. P., & Peltier, W. R. (1991). The influence of stratification on secondary instability in free shear layers. *Journal of Fluid Mechanics*, *227*, 71–106.

Lelong, M.-P., & Dunkerton, T. J. (1998). Inertia-gravity wave breaking in three dimensions. Part I: Convectively stable waves. *Journal of the Atmospheric Sciences*, *55*, 2473–2488. https://doi.org/10.1175/1520-0469(1998) 055

Li, F., Liu, A. Z., Swenson, G. R., Hecht, J. H., & Robinson, W. A. (2005). Observations of gravity wave breakdown into ripples associated with dynamical instabilities. *Journal of Geophysical Research*, *110*, D09S11. https://doi.org/10.1029/2004JD004849

Lombard, P. N., & Riley, J. J. (1996). Instability and breakdown of internal gravity waves. I. Linear stability analysis. *Physics of Fluids*, *8*, 3271–3287. https://doi.org/10.1063/1.869117

Martinis, C. R., Baumgardner, J., Smith, S. M., Colerico, M., & Mendillo, M. (2006). Imaging science at El Leoncito, Argentina. *Annales de Geophysique*, *24*, 1–12.

Mertens, C. J., Mlynczak, M. G., Löpez-Puertas, M., Wintersteiner, P. P., Picard, R. H., Winick, J. R., … Russell III, J. M. (2001). Retrieval of mesospheric and lower thermospheric kinetic temperature from measurements of CO_2 15 μm Earth limb emission under non-LTE conditions. *Geophysical Research Letters*, *28*(7), 1391–1394.

Miller, A. D., Fritts, D. C., Chapman, D., Jones, G., Limon, M., Araujo, D., … Wang, L. (2015). Stratospheric imaging of polar mesospheric clouds: A new window on small-scale atmospheric dynamics. *Geophysical Research Letters*, *42*, 6058–6065. https://doi.org/10.1002/2015GL064758

Minzner, R. A. (1977). The 1976 standard atmosphere and its relationship to earlier standards. *Reviews of Geophysics*, *15*(3), 375–384. https://doi.org/10.1029/RG015i003p00375

Orlanski, I., & Bryan, K. (1969). Formation of the thermocline step structure by large-amplitude internal gravity waves. *Journal of Geophysical Research*, *74*(28), 6975–6983. https://doi.org/10.1029/JC074i028p06975

Pitteway, M. L. V., & Hines, C. O. (1963). The viscous damping of atmospheric gravity waves. *Canadian Journal of Physics*, *41*, 1935–1948.

Preusse, P., Dörnbrack, A., Eckermann, S. D., Riese, M., Schaeler, B., Bacmeister, J. T., … Grossmann, K. U. (2002). Space based measurements of stratospheric mountain waves by CRISTA: 1. Sensitivity, analysis method and a case study. *Journal of Geophysical Research*, *107*(D23), 8178. https://doi.org/10.1029/2001JD000699

Russell, J. M., Mlynczak, M. G., Gordley, L. L., & Tansock, J. (1999). An overview of the SABER experiment and preliminary calibration results. *Proceedings of SPIE — The International Society for Optical Engineering*, *3756*, 277–288.

Sato, K., Tateno, S., Watanabe, S., & Kawatani, Y. (2012). Gravity wave characteristics in the Southern Hemisphere revealed by a high-resolution middle-atmosphere general circulation model. *Journal of the Atmospheric Sciences*, *69*, 1378–1396.

Singer, B. A., & Joslin, R. D. (1994). Metamorphosis of a hairpin vortex into a young turbulent spot. *Physics of Fluids*, *6*, 3724–3736.

Smith, A. K. (2012). Global dynamics of the MLT. *Surveys in Geophysics*, *33*(6), 1177–1230. https://doi.org/10.1007/s10712-012-9196-9

Smith, S., Baumgardner, J., & Mendillo, M. (2009). Evidence of mesospheric gravity-waves generated by orographic forcing in the troposphere. *Geophysical Research Letters*, *36*, L08807. https://doi.org/10.1029/2008GL036936

Smith, S. M., Scheer, J., Reisin, E. R., Baumgardner, J., & Mendillo, M. (2006). Characterization of exceptionally strong mesospheric wave events using all-sky and zenith airglow observations. *Journal of Geophysical Research*, *111*, A09309. https://doi.org/10.1029/2005JA011197

Sonmor, L. J., & Klaassen, G. P. (1997). Toward a unified theory of gravity wave stability. *Journal of the Atmospheric Sciences*, *54*, 2655–2680. https://doi.org/10.1175/1520-0469(1997)054<2655:TAUTOG>2.0.CO;2

Swenson, G. R., & Liu, A. Z. (1998). A model for calculating acoustic gravity wave energy and momentum flux in the mesosphere from OH airglow. *Geophysical Research Letters*, *25*(4), 477–480.

Taylor, M. J., Gardner, L. C., & Pendleton, Jr. W. R. (2001). Long period wave signatures in mesospheric OH Meinel (6,2) band intensity and rotational temperature at mid latitudes. *Advances in Space Research*, *27*(6–7), 1171–1179.

Theodorsen, T. (1952). *"Mechanism of turbulence," in Proceedings of the 2nd Midwestern Conference on Fluid Mechanics*. Columbus, OH: Bulletin No 149 Ohio State University.

Thorpe, S. A. (1973). Experiments on instability and turbulence in a stratified shear flow. *Journal of Fluid Mechanics*, *61*, 731–751.

Vadas, S. L., & Fritts, D. C. (2005). Thermospheric responses to gravity waves: Influences of increasing viscosity and thermal diffusivity. *Journal of Geophysical Research*, *110*, D15103. https://doi.org/10.1029/2004JD005574

Walterscheid, R. L., Gelinas, L. J., Hecht, J. H., & Liu, A. Z. (2013). Instability structures during periods of large Richardson number ($Ri > 1/4$): Evidence of parametric instability. *Journal of Geophysical Research: Atmospheres*, *118*, 6929–6939. https://doi.org/10.1002/jgrd.50514

Walterscheid, R. L., & Schubert, G. (1990). Nonlinear evolution of an upward propagating gravity wave: Overturning, convection, transience, and turbulence. *Journal of the Atmospheric Sciences*, *47*, 101–125.

Werne, J., & Fritts, D. C. (1999). Stratified shear turbulence: Evolution and statistics. *Geophysical Research Letters*, *26*, 439–442. https://doi.org/10.1029/1999GL900022

Yamada, Y., Fukunishi, H., Nakamura, T., & Tsuda, T. (2001). Breaking of small-scale gravity wave and transition to turbulence observed in OH airglow. *Geophysical Research Letters*, *28*, 2153–2156.